치의과학 박사학위논문

칼슘감지 수용체를 통한 mineral trioxide aggregate 의 세포 내 작용 기전

G-protein coupled calcium-sensing receptor-mediated modulatory mechanisms of mineral trioxide aggregate

2017 년 8 월

서울대학교 대학원

치의과학과 신경생물학 전공

최 슬 기

Abstract

G-protein coupled calcium-sensing receptor-mediated modulatory mechanisms of mineral trioxide aggregate

Seulki Choi
Program in Neuroscience
The Graduate School
Seoul National University

Mineral trioxide aggregate (MTA) is a calcium silicate-based bioactive material that has been extensively used in dentistry. MTA has been associated with excellent clinical outcomes in the repair of damaged pulp and periapical tissues and has also been the material of choice for pulp capping and perforation repair. Moreover, MTA has recently started to be applied in regenerative dental therapies that aim to regenerate vasculatures in the pulp space to promote the root formation of immature teeth in a process referred to as pulp revascularization. These clinical effects are partly due to the advanced physical properties of MTA, e.g., good sealing ability, optimal strength and hardness, and compatibility with humidity. MTA is known to induce diverse cellular functions such as proliferation, cytokine production/release, and

differentiation; these functions play a pivotal role in biomineralization and tissue repair/regeneration in biological systems. However, limited insight into the intracellular signaling pathways has been provided to explain the biological activities of MTA. Therefore, doing a research on identifying the signal transduction mechanism of MTA in human dental pulp cells (hDPCs) withholds a great significance and it has the potential evidences for developing novel biomaterials for regenerative dental therapy.

In this work, I revealed upstream mediator and the origin of the intracellular Ca^{2+} response upon MTA treatment that are yet undiscovered. I examined the effect of MTA on intracellular Ca^{2+} ($[Ca^{2+}]_i$) in hDPCs by live cell imaging and elucidate the MTA-induced Ca^{2+} mobilization from endoplasmic reticulum (ER). Especially, I found the molecular mediator of MTA was G protein-coupled calcium sensing receptor (CaSR). In addition, MTA-induced extracellular changes of Ca^{2+} and pH synergistically activate CaSR. Finally, My research showed that CaSR translates the signaling input from MTA into diverse downstream pathways and also demonstrated that the MTA-mediated CaSR signaling exert a critical role in osteogenic differentiation of hDPCs. Based on these data, I propose a model based on the CaSR signaling cascade to explain the mechanism of MTA.

In conclusion, through this paper, signal transduction mechanism of MTA was identified. I firstly elucidate that the CaSR is a major signaling mediator of MTA-induced biological effects. These findings suggest that potential evidences for developing novel biomaterials for regenerative dental therapy.

Key Words: Mineral trioxide aggregate, Calcium-sensing receptor, Ca^{2+}, pH, Osteogenic differentiation, Human dental pulp cells

Student Number: 2010-23777

Contents

Abstract ---------- **I**

Contents ---------- **IV**

List of Figures ---------- **VI**

Abbreviations ----------**VIII**

Purpose ---------- **1**

Introduction ---------- **2**

Materials and Methods ---------- **11**

Reagents and plasmid ---------- 11
Human dental pulp cells (hDPCs) culture and transfection ---- 12
Immuno-phenotyping of hDPCs ---------- 13
Preparation of MTA solution ---------- 14
Cell viability test ---------- 14
Live cell imaging and Ca^{2+} measurements ---------- 15
pH measurements ---------- 16
RT-PCR and real-time PCR ---------- 16
Immunofluorescence ---------- 18
Western blot ---------- 19
Alizarin red S (ARS) staining and Alkaline phosphatase (ALP)
activity measurement ---------- 20
Statistical analysis ---------- 21

Results ---------- **22**

Human dental pulp cells (hDPCs) isolation and characterization -- 22
Ca^{2+} concentration and pH value of MTA ---------- 24
The Effect of MTA on intracellular Ca^{2+} ($[Ca^{2+}]_i$) in hDPCs ----- 26
Identifying the origin of MTA-induced intracellular
Ca^{2+} mobilization ---------- 28
Calcium-sensing receptor (CaSR) identification in hDPCs ------- 32
CaSR is a crucial mediator of MTA-mediated intracellular
signaling pathway ---------- 36
Distinct effects of MTA-mediated Ca^{2+} and pH modulation
on CaSR signaling dynamics ---------- 41
Effect of pH_e alteration on CaSR signaling kinetics ---------- 48
Effect of MTA on NFAT activity ---------- 50
Involvement of CaSR-NFAT signaling cascade on MTA-
induced osteogenic differentiation ---------- 52

Discussion ---------- **59**

References ---------- **65**

Conclusion ---------- **76**

Abstract in Korean ---------- **78**

List of Figures

Figure 1. Images from regenerative endodontic procedures ---------- 5
Figure 2. Schematic representation of calcium-sensing receptor (CaSR) - 10
Figure 3. Stem cell phenotype of human dental pulp cells (hDPCs) ----- 23
Figure 4. Ca^{2+} concentration and pH value of MTA ---------- 25
Figure 5. MTA increase intracellular Ca^{2+} ($[Ca^{2+}]_i$) in hDPCs ---------- 27
Figure 6. MTA induced intracellular Ca^{2+} mobilization from endoplasmic reticulum (ER) ---------- 30
Figure 7. Expression of CaSR in hDPCs ---------- 34
Figure 8. Intracellular localization of CaSR in hDPCs ---------- 35
Figure 9. NPS2143 inhibits MTA-induced $[Ca^{2+}]_i$ increase ---------- 38
Figure 10. U73122 inhibits MTA-induced $[Ca^{2+}]_i$ increase ---------- 39
Figure 11. NPS2143 inhibits MTA-induced phosphoinositide 3-kinase (PI3K) activity and ERK phosphorylation ---------- 40
Figure 12. The individual effects of Ca^{2+} and alkaline pH release from MTA on $[Ca^{2+}]_i$ response ---------- 43
Figure 13. Neutral pH of MTA is significantly reduced $[Ca^{2+}]_i$ response --- 44
Figure 14. NPS2143 inhibits alkaline pH-induced $[Ca^{2+}]_i$ increase ------- 45
Figure 15. $[Ca^{2+}]_i$ and pH_i was not affected by experimental solutions -- 46
Figure 16. Kinetics of pH_e alteration in hDPCs ---------- 48
Figure 17. Suggested pathway of MTA-induced osteoblast differentiation - 50
Figure 18. MTA activated nuclear factor of activated T cells (NFAT) translocation ---------- 51
Figure 19. Expression patterns of osteoblastic makers during inhibition of CaSR-NFAT signaling cascade ---------- 54

Figure 20. Expression patterns of osteogenic/odontogenic markers during differentiation ---------- 56
Figure 21. CaSR-NFAT signaling cascade regulates MTA-induced mineralization ---------- 58
Figure 22. Schematic representation of MTA-mediated signaling pathways ----------77

Abbreviations

MTA	Mineral trioxide aggregate
CaSR	Calcium sensing receptor
hDPCs	Human dental pulp cells
ER	Endoplasmic reticulum
PLC	Phospholipase C
PI3K	Phosphoinositide-3 kinase
NFAT	Nuclear factor of activated T cells
$[Ca^{2+}]_i$	Intracellular Ca^{2+}
$[Ca^{2+}]_e$	Extracellular Ca^{2+}
pH_i	Intracellular pH
pH_e	Extracellular pH
SF	Serum-free media
OM	Osteogenic differentiation media
Tg	Thapsigargin
CsA	Cyclosporin

Purpose

For over two decades, MTA has been extensively use in clinical dentistry. MTA has been highlighted in its diverse biological functions and excellent clinical outcomes. Despite of such long-term application, the molecular mechanism of MTA is still largely unknown, unfortunately. The insufficient scientific background about complex MTA biochemistry could bring out potential toxicity or unwanted consequence due to the unknown chemical reaction or ingredients of MTA. Meanwhile, a number of researchers have been tried to improve MTA's biological effect and physical properties. In this respect, I tried to investigate the molecular mechanisms of MTA in hDPCs. To archive this goal, I performed sequential experiments with the following three aims:

1. To investigate the intracellular Ca^{2+} signaling of MTA in hDPCs
2. To determine the mediator of MTA in hDPCs
3. To elucidate the relationship between biological function of MTA and involvement of signaling pathway

This thesis addressed the specific aims described above.

Introduction

1. Mineral trioxide aggregate (MTA)

Mineral trioxide aggregate (MTA) was first described in the scientific lecture in 1993 as a root-end filling material due to its hydraulic properties (Lee et al., 1993). Most dental materials exhibit a deterioration in physical properties upon contact with moisture. Thus, a hydraulic material was introduced in order to counteract this problem. The first US patent (Torabinejad et al., 1995; Torabinejad et al., 1998) drawn for MTA explains this invention saying "Due to the presence of blood and moisture, the mouth is a less than ideal environment for many materials which could otherwise be useful as dental filling and sealing materials".

1.1. Composition of MTA

MTA is composed of a mixture of Portland cement and bismuth oxide. The bismuth oxide is added to the cement to enhance the radiopacity of the material. The Portland cement component in MTA is mainly consists of diclacium silicate, tricalcium silicate, tricalcium aluminate and tetracalcium aluminoferrite (Parirokh and Torabinejad, 2010b). Tricalcium silicate is major

component in the formation of calcium silicate hydrate which gives early strength.

1.2. Setting reactions of MTA

MTA is a hydraulic type of materials, meaning that is sets by reacting with water, and is then stable in water. Upon hydration, MTA form a colloidal gel to a hard structure, with moisture from the surrounding tissues assisting the setting reaction (Lee et al., 1993). Hydrated MTA releases Ca^{2+} ions constantly, thereby forming calcium hydroxide in a silicate matrix (Camilleri et al., 2005; Camilleri, 2007). This chemical compound acts as a source from which Ca^{2+} and hydroxide ions are released to the surrounding environment. Hydrated MTA has been reported to have a highly alkaline pH for a long duration after the setting reaction (Fridland and Rosado, 2005). Moreover, the Ca^{2+} concentration surrounding the material is elevated after setting (1 mg/dL) (Duarte et al., 2003). These two factors, Ca^{2+} and pH, have been regarded as the primary factors evoking biological responses (Sangwan et al., 2013)

1.3. Clinical application of MTA

MTA has been associated with excellent clinical outcomes in the repair of damaged pulp and periapical tissues and has also been the material of choice

for pulp capping, root canal filling and repair of root perforation (Parirokh and Torabinejad, 2010a). Moreover, MTA has recently started to be applied in regenerative dental therapies that induces regeneration of vasculatures in the pulp space for promoting for promoting immature root structures in a process referred to as pulp revascularization (Wigler et al., 2013; Law, 2013) (Fig. 1). These clinical effects are partly due to the advanced physical properties of MTA, e.g., excellent biocompatibility, compatibility to humidity, good sealing ability, optimal strength, hardness and compatibility with humidity (Parirokh and Torabinejad, 2010b)

1.4. Biological functions of MTA

Up to date, MTA has been known to induce diverse biological functions such as proliferation, cytokine production/release, and differentiation; these functions play a crucial role in biomineralization and tissue repair/regeneration in biological systems (Torabinejad and Parirokh, 2010). Hydration of MTA release Ca^{2+} and hydroxide ions, and the changes of these factors induces the transcriptional changes, then differentiates the cells to osteo / odontogenic phenotypes. However, the upstream signaling mechanism of MTA is still largely unknown, unfortunately.

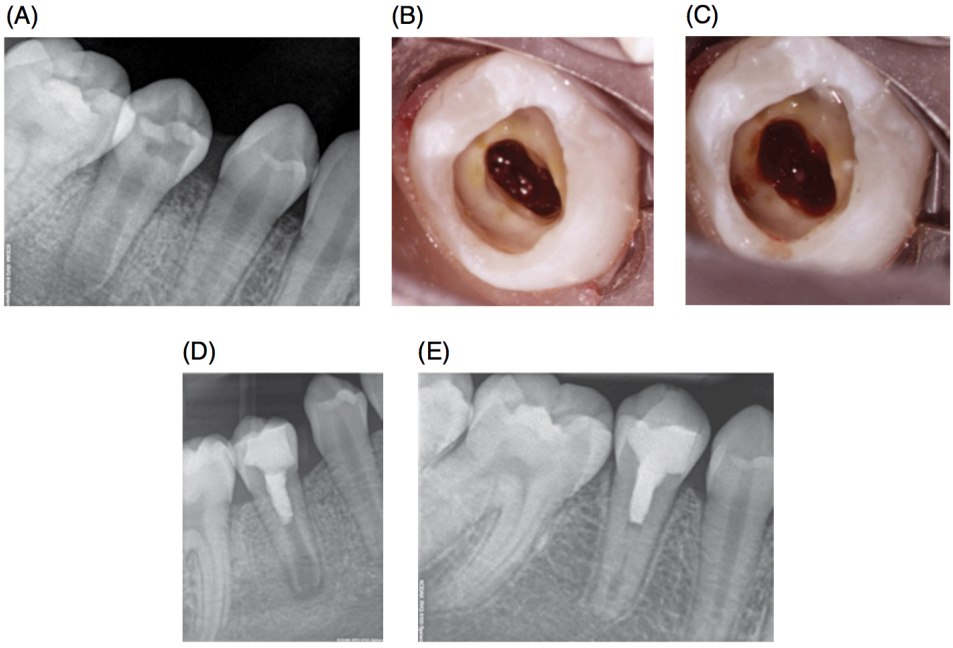

Figure 1. Images from regenerative endodontic procedures.

(A) A preoperative radiograph of a mandibular second premolar with an open apex, necrotic pulp, and a periapical lesion. (B) An access cavity is made into the root canal of this tooth, which contains a necrotic pulp. (C) After cleaning and disinfecting the canal, bleeding is generated inside the canal. (D) A layer of MTA is placed over the blood clot. (E) A radiograph taken 15 months later shows resolution of the periapical lesion and thickening of the root canal walls (Law, 2013).

2. Calcium-sensing receptor (CaSR)

Calcium is a well-characterized and important intracellular second messenger (Berridge et al., 2000). In addition, calcium ions also have essential roles as extracellular messengers, mainly via the binding to extracellular calcium-sensing receptors (CaSR) (Hofer and Brown, 2003). The CaSR is a large glycoprotein that belongs to family C of G protein-coupled receptors (GPCR) (Brown and MacLeod, 2001).

The CaSR is unique in the GPCR superfamily for several reasons: First, while the majority of the Group C family members have two or more isoforms, there is only one gene product known to yield transcripts sensing Ca^{2+}/cation (Brown et al., 1993). Although, recently another family C GPCR, GPRC6A, was found to sense extracelluar Ca^{2+} ($[Ca^{2+}]_e$), albeit at levels well above those present in various extracellular fluid (Pi et al., 2005) it is however currently conjectural whether GPCR6A qualifies as a *bona fide* CaSR. Second, unlike many GPCRs the CaSR is resistant to desensitization, as would be appropriate for its continuous surveillance of $[Ca^{2+}]_e$ levels. Third, the apparent affinity of the receptor for $[Ca^{2+}]_e$ is within the millimolar range, which is rather low when compared with other GPCRs, which normally exhibit EC_{50} values for

their ligands within the nano- to submicromolar concentration range (Conigrave et al., 2000).

2.1. Functional expression of CaSR

CaSR was first cloned from bovine parathyroid glands (Brown et al., 1993), where it controls parathyroid hormone (PTH) secretion in response to changes in extracellular ionized calcium concentration. CaSR expression and functions has also been reported in diverse organs involved in maintaining Ca^{2+} homeostasis, both directly and indirectly, including the kidney, breast, nervous system, and bone (Mango et al., 2004). Especially, CaSR has been known to regulate bone remodeling; CaSR activation induced osteoblast proliferation (Dvorak et al., 2004), and CaSR knock-out mice exhibited under mineralization phenotypes in developing skeletal system (Chang et al., 2008; Sun et al., 2010)

2.2. CaSR modulator

The CaSR can respond to subtle changes of extracellular Ca^{2+} (i.e., on a micromolar scale) and also interacts promiscuously with various polycations (e.g., Mg^{2+} and Gd^{3+}) and polyamines that activate the receptor with different amplitude (Handlogten et al., 2000; Hofer and Brown, 2003).

The CaSR can also sense ionic strength. That is, exposing bovine parathyroid cells to increased ionic strength by adding 40 mM NaCl to that already present in the ambient medium (e.g., ~140 mM NaCl) increases the EC_{50} for $[Ca^{2+}]_o$-induced inhibition of PTH secretion by nearly ~40% (Quinn et al., 1998). Changes in ionic strength can alter the electrical field surrounding polycationic CaSR agonists, thus providing a potential mechanism for modulating their activation of the CaSR.

Furthermore, several CaSR-expressing tissues, including regions of the stomach, the kidney, bone and the brain, could potentially use the CaSR as a sensor for pH. Indeed, increases or decreases in pH, within the range of 6 - 8.5, increase or decrease, respectively, the receptor's sensitivity to $[Ca^{2+}]_e$ and $[Mg^{2+}]_e$ (Quinn et al., 2004)

2.3. CaSR signaling cascades

Elevations in the extracellular Ca^{2+}, or exposure to other CaSR agonists, activated CaSR translates the signaling input into multiple downstream pathways such as the phospholipase C (PLC), mitogen-activated protein kinase (MAPK), and phosphoinositide-3 kinase (PI3K) pathways. This signaling is mediated by interactions with $G_{q/11}\alpha$ subunits and the

corresponding effectors for each signaling pathway (Handlogten et al., 2001) (Fig. 2). Given its ability to respond to extracellular environmental changes, CaSR acts as a versatile sensor and regulator to maintain physiological balance in biological systems.

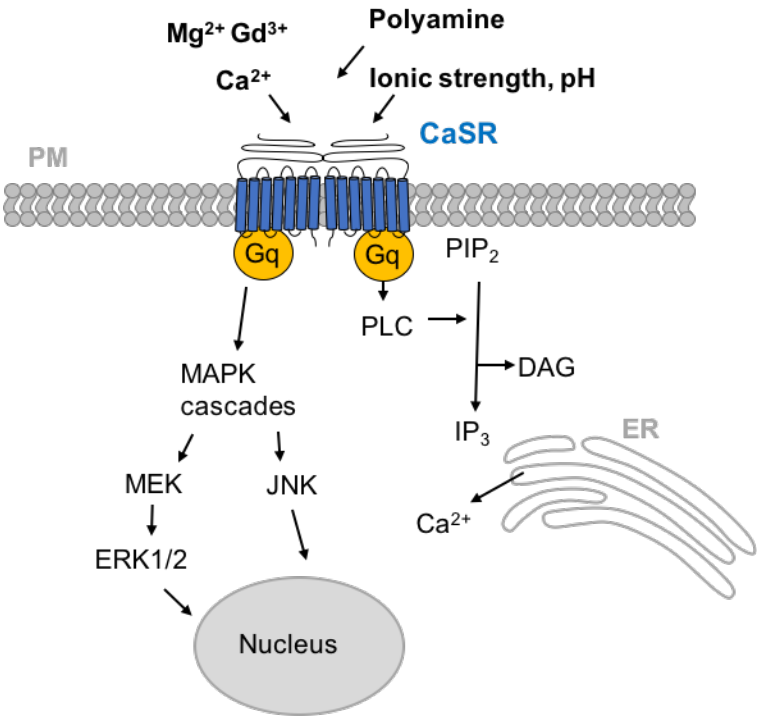

Figure 2. Schematic representation of calcium-sensing receptor (CaSR).

Numerous agonists converge on the extracellular calcium-sensing receptor (CaSR) to activate a complex network of intracellular signal-transduction cascades.

Materials and Methods

Reagents and plasmids

The following reagents were used at the indicated concentrations in this experiments: 100 μM $LaCl_3$ (449830, Sigma), 1 μM thapsigargin (T9033, Sigma), 1 μM SKF 96365 (S7809, Sigma), 100 μM streptomycin (S6501, Sigma), 100 μM nifedifine (N7634, Sigma), 1-10 μM NPS 2143 (3626, Tocris), 1 μM U-73122 (U6756, Sigma), 1-10 μM cyclosporin A (30024, Sigma), and 1 μM ER-Tracker Red (E34251, Invitrogen).

The following plasmids were purchased from Addgene: CMV-R-GECO1 was a gift from Robert Campbell (Addgene plasmid # 32444) (Zhao et al., 2011), pGP-CMV-GCaMP6s was a gift from Douglas Kim (Addgene plasmid # 40753) (Zhao et al., 2011), and pGP-CMV-GCaMP6s-CAAX was a gift from Tobias Meyer (Addgene plasmid # 52228) (Zhao et al., 2011). The generation procedures of dTomato-PH_{AKT1} and NFATc1-mCherry constructs were described previously (Kim et al., 2014; Kyung et al., 2015).

Human dental pulp cells (hDPCs) culture and transfection

Human third molars without caries and infection were collected from six patients (18-22 years of age) at Kyung Hee University Dental Hospital (Seoul, Korea). The experimental protocol was approved by the Institutional Review Board of Kyung Hee University Dental Hospital (KHD IRB 1606-1), and all patients provided informed consent. hDPCs were isolated as described previously (Lee et al., 2011). Briefly, the coronal part of the tooth was removed with a high-speed handpiece equipped with a surgical bur, and the pulp tissue was extracted gently with forceps. The extracted pulp tissue was then minced with a surgical blade and placed in 60-mm culture dishes. The explants were cultured in DMEM (LM 001-05, Welgene) supplemented with 10% FBS (S 001-07, Welgene) and 1% penicillin/streptomycin (15140-22, Gibco) at 37°C with 5% CO_2. Cells were used from passages 4 - 9 for all experiments. hDPCs were transfected with Lipofectamine 2000 (11668-030, Invitrogen) according to the manufacturer's instructions. Transfected cells were plated on a 96-well glass bottom plate (0611129L2L, Matrical Bioscience) coated with poly-D-lysine hydrobromide (P6407, Sigma). The cells were incubated for 24 h before each experiment.

Immuno-phenotyping of hDPCs

To characterize the phenotype of the hDPCs, I used antibodies against various cell-surface markers and flow cytometry (Beckman Coulter, Miami, FL, USA, excitation laser 488 nm). Samples were incubated with Human Fc Receptor Binding Inhibitor (eBioscience, 14-9161-73; 20 µl). Antibodies against the mesenchymal stem cell surface markers FITC-conjugated PerCP-CyTM5.5 anti-human CD146 (BD Biosciences, 562134; 5 µl), PE anti-human CD105 (BD Biosciences, 560839; 5 µl), PE anti-human CD90 (R&D Systems, FAB2067P; 5 µl) and FITC anti-human CD73 (BD Biosciences, 561254; 5 µl) were used. Antibodies against the hematopoietic origin surface markers PE anti-human CD34 (Invitrogen, CD34-581-04; 5 µl) and FITC anti-human CD45 (BD Biosciences, 555482; 20 µl) were used to exclude a hematopoietic origin. At least 5 x 10^4 events were recorded by flow cytometry, and data were analyzed with FlowJo software (FlowJo, Ashland, OR, USA).

Preparation of MTA solution

A total of 0.2 g of MTA powder (ProRoot MTA, Dentsply and MTA Angelus, Angelus) was diluted with 20 ml DMEM or normal HEPES buffer (pH 7.4) containing 140 NaCl, 5 KCl, 1 $MgCl_2$, 1 $CaCl_2$, 10 D-glucose, and 10 HEPES-Na (in mM). The mixture was incubated for 24 h at 37°C in a shaking incubator and then filtered through a 0.2 μm pore filter (16534-K, Sartorius). To measure the Ca^{2+} concentrations of experimental solutions containing MTA, a colorimetric Calcium Detection Kit (ab102505, Abcam) was used. Briefly, the calcium reagent working solution was added to each sample according to the manufacturer's instructions, and the absorbance was measured at 575 nm using a multi-detection microplate reader (Synergy 2, BioTek). The pH of the MTA solution was measured using a pH meter (8157BNUMD, ThermoFisher).

Cell viability test

Cell viability was determined using a Cell Counting Kit-8 (CCK-8; CK04, Dojindo Molecular Technologies). Briefly, cells were plated in 96-well plates at a density of 2×10^4 cells per well and cultured in growth medium. The cell numbers in triplicate wells were measured as the absorbance (450 nm) of reduced WST-8.

Live cell imaging and Ca^{2+} measurements

Prepared cells were plated on 96-well glass-bottom plates (Matrical Bioscience) for live cell imaging, conducted with a laser scanning confocal microscope (LSM 700, Carl Zeiss). Lasers with 405 nm (blue), 488 nm (green), and 595 nm (red) excitation wavelengths were used for acquisition of multicolor images. Images were analyzed with Zen 2010 software (Zeiss). To perform intracellular Ca^{2+} ($[Ca^{2+}]_i$) measurements under a perfusion system, hDPCs were seeded on 15-mm glass coverslips (5×10^4 cells/coverslip) and incubated for 24 hr. Next, the cells were loaded with DMEM containing 2 μM Fura-2/AM (F1201, Invitrogen) for 20 min at room temperature. During live imaging, the cells were maintained at 37 °C in a customized perfusion chamber (Live Cell Instrument). Fluorescence ratios were monitored through an Olympus IX71 microscope equipped with a rapidly switchable Xenon lamp (LAMBDA DG-4, Sutter Instrument Company) with dual excitation at 340 and 380 nm and emission at 510 nm. A MetaFluor imaging system (version 6.1, Universal Imaging) was used for recording and analysis. Results are presented as *F*340/380 ratio.

pH measurements

Intracellular pH (pH_i) measurements were performed as described previously (Namkoong et al., 2015). Briefly, hDPCs were seeded on 15-mm glass coverslip (5×10^4) and then incubated for 24 hr. Next, cells were loaded with DMEM containing 2 μM BCECF-AM (B1150, Invitrogen) for 20 min at room temperature. Approximately 15–20 cells in the imaging perfusion chamber were recorded at 37 °C and analyzed in each experiment. The standard HCO_3^--buffered solution (pH 7.4) contained 10 D-glucose, 10 HEPES, 115 NaCl, 5 KCl, 1 $MgCl_2$, 1 $CaCl_2$, and 25 $NaHCO_3$ (in mM). For intracellular acidification, cells were perfused with 20 mM NH_4Cl in a standard HCO_3^--buffered solution. Fluorescence ratios were monitored through an Olympus IX71 microscope equipped with a rapidly switchable Xenon lamp with dual excitation at 440 and 490 nm and emission at 530 nm. Results are presented as *F*440/490 ratio.

RT-PCR and real-time PCR

Total RNA was isolated using the RNeasy Mini Kit (74140, Qiagen). Reverse transcriptase was used with an oligo-dT primer (18080-051, Invitrogen) to prepare cDNA from 1 μg of total RNA. PCR was performed with 1 μL of cDNA and previously reported primers (Koori et al., 2014; Li et al., 2015).

The cycling parameters were as follows: 35 cycles of denaturation at 95°C for 30s, annealing for 30s, and extension at 72°C for 30s, followed by a final extension step at 72°C for 10 min. PCR products were resolved using an electrophoresis system (Mupid®-2 plus, OPTIMA) on 1% agarose gels containing 0.1 μg/mL ethidium bromide (E8751, Sigma) and were visualized under UV light with a transilluminator (TS-312R, Spectroline). Quantitative real-time PCR was performed using cDNA and SYBR PCR master mix (4309155, Applied BioSystems). Samples were analyzed with Applied Biosystems 7200 instrument. All PCRs were performed in at least duplicate, and the specificity of each reaction was confirmed by melting curve analysis at the dissociation stage. The following PCR primer sequences were used: GAPDH forward, 5'- TCA ACG ACC ACT TTG TCA AGC TCA -3'; GAPDH reverse, 5'- GCT GGT GGT CCA GGG GTC TTA CT -3'; CaSR forward, 5'- TCC ACG GTC AGA TTT GCT GTT C -3'; CaSR reverse, 5'- TTG ATG TCC CAT CAG TCT GCA C -3'; BMP-2 forward, 5'- AGC GAG TTC GAG TTG CGG CT -3'; BMP-2 reverse, 5'- AGC TGC GCA CAG TGT TGG CT -3'; RUNX2 forward, 5'- AAC CCT TAA TTT GCA CTG GGT CA -3'; RUNX2 reverse, 5'- CAA ATT CCA GCA ATG TTT GTG CTA C -3'; OCN forward, 5'- CCC AGG CGC TAC CTG TAT CAA -3'; OCN reverse, 5'- GGT CAG CCA ACT CGT CAC AGT C -3'; OPN forward, 5'- ACA

CAT ATG ATG GCC GAG GTG A -3'; OPN reverse, 5'- TGT GAG GTG ATG TCC TCG TCT GTA G -3'; COL3A1 forward, 5'- GTG GAC CTG GTG CTG CTG -3'; COL3A1 reverse, 5'- GGG TCC TGG GTT ACC ATT ACT AC -3'; DSPP forward, 5'- TTC CGA TGG GAG TCC TAG TG -3'; DSPP reverse, 5'- TGA GCT TCT GGG TGT CCT CT -3'; DMP1 forward, 5'- CCT GAG GAT GAG AAC AGC TCC A -3'; DMP1 reverse, 5'- GAT CTG CTG CTG TCT TGA GAG TCA C -3'.

Immunofluorescence

hDPCs were seeded in 96-well plates (2 x 10^4 cells/well) and incubated for 24 hr. Cells were then fixed in 4% paraformaldehyde at room temperature for 15 min, and then washed in PBS. For permeabilization, cells were incubated in PBS containing 1% Triton X-100 for 10 min at room temperature, and then incubated in blocking solution consisting of PBS with 10% normal donkey serum for 1 hour at room temperature. Next, the cells were stained with rabbit anti-CaSR (1:200; ab18200, Abcam), goat anti-BMP-2 (1:100; sc-6895, Santa Cruz Biotech), mouse anti-PMCA (1:200; sc-271194) and mouse anti-GM130 (1:200; BD Biosciences, 610822) followed by Alexa Fluor 488 donkey anti-

rabbit IgG antibodies (1:200; A-11008, Invitrogen), Alexa Fluor 488 donkey anti-goat IgG antibodies (1:200; A-11055, Invitrogen) and Alexa Fluor 594 goat anti-mouse IgG antibodies (1:200; A-11032, Invitrogen). Finally, cells were mounted with Vectashield mounting medium (H-1200, Vector Laboratories) and visualized using a laser scanning confocal microscope (LSM 700, Carl Zeiss).

Western blot

hDPCs were sonicated in RIPA buffer (R4200-010, GenDEPOT). The samples were centrifuged at 13,000 rpm at 4°C, and the supernatants were subjected to SDS/PAGE and immunoblotting. Protein concentrations were measured using the Nanodrop Spectrophotometer (ND-1000, Thermo Scientific). Protein samples were resolved on 10 % SDS-PAGE gels (Bio-Rad Laboratories). After electrophoretic separation using a iBLOT 2 Dry Blotting system (IB21001, Thermo Scientific), the proteins were transferred to nitrocellulose membranes. The membranes were then blocked with 10 % non-fat milk and incubated with anti-ERK antibodies (1:1000; 9102, Cell signaling) and anti-pERK antibodies (1:1000; 9101, Cell signaling). After washing, membranes were then incubated with anti-rabbit IgG-HRP (1:5000; sc-2030. Santa Cruz Biotech). Immunoreactive bands were ultimately visualized using

ECL reagents (32106, Thermo Scientific) and detected with Chemidoc XRS+ system (Bio-Rad Laboratories).

Alizarin red S (ARS) staining and alkaline phosphatase (ALP) activity measurement

Osteogenic differentiation was determined by ARS and ALP staining. hDPCs were prepared on 24-well plates at a density of $5\times10^4/cm^2$ in differentiation media [DMEM supplemented with 10% FBS, 1% penicillin/streptomycin, 50 μg/ml ascorbic acid, and 10 mM β-glycerophosphate (G9422, Sigma)] for 21 days with MTA in the presence or absence of inhibitors. For ARS staining, the cell layer was washed with PBS and fixed in 4% PFA for 20 min at room temperature. Fixed cells were then stained with 1% alizarin red-S (pH 4.2; A5533, Sigma) for 20 min at room temperature and visualized using a stereo-zoom microscope (Leica S6D). ALP activity was measured using microplate reader with Alkaline Phosphatase Yellow Liquid Substrate System (P7998, Sigma). After 21 days of culture, cells were collected and homogenized in 10 mM Tris-HCl buffer (pH 7.4) using a sonicator and then centrifuged. Then, the working solution was added to the cell lysate according to the manufacturer's protocol and incubated at 37°C for 30 min. The reaction was stopped with 3N NaOH, and the absorbance was measured at 405 nm.

Statistical analysis

Data are presented as mean ± SEM or median ± min/max. Statistical analyses were completed with Microsoft Excel. Statistical significance between two groups was evaluated by two-tailed student's *t*-test. Multiple comparisons were performed using one-way analysis of variance (ANOVA), and pairwise differences between groups were determined using a two-tailed *t*-test with Bonferroni correction. For each experiment, at least two biological replicates were performed.

Results

Hunam dental pulp cells (hDPCs) isolation and characterization

The stem cell characteristics of the human dental pulp cells (hDPCs) used in this study were characterized by analyzing the expression of mesenchymal stem cell (MSC) surface markers through flow cytometry (Fig. 3). Phenotypic FACS analysis showed that hDPCs stably expressed mesenchymal markers (CD90, CD73, and CD105) and surface adhesion molecules (CD146), while they did not display any hematopoietic molecular markers (CD34, and CD45).

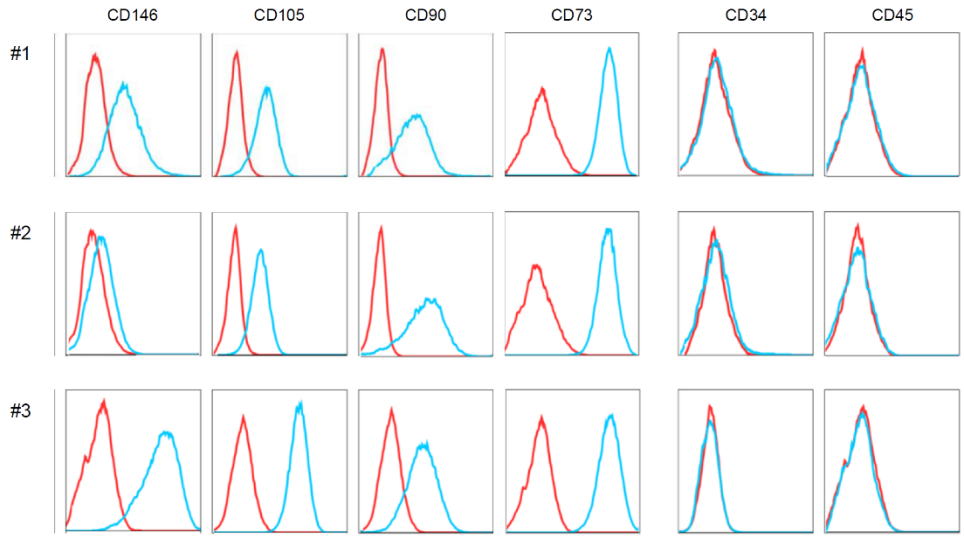

Figure 3. Stem cell phenotype of human dental pulp cells (hDPCs).

Stem cell phenotype of hDPCs from three patients (#1-3). Cells were stained with antibodies against CD 146 (surface adhesion molecule), CD 105, CD 90, CD 73 (mesenchymal marker), CD 34, and CD 45 (hematopoietic molecular marker), and changes in expression profiles were analyzed by flow cytometry.

Ca^{2+} concentration and pH value of MTA

Mineral trioxide aggregate (MTA) consists mainly of calcium oxide and silicate derivatives, which are converted to calcium hydroxide upon contact with tissue fluid. This calcium hydroxide constantly releases calcium and hydroxide ions. Based on this biochemical property of MTA, I measured the Ca^{2+} concentrations and pH values of the experimental solutions containing calcium silicate-based biomaterials (ProRoot MTA and MTA-Angelus). The measured pH values and Ca^{2+} concentrations of the HEPES (4-(2-hydroxyethyl)-1-piperazineethanesulfonic acid) solutions containing MTA were similar to those previously reported [pH: 9.32 (ProRoot) and 9.28 (Angelus), Ca^{2+} concentration: 1.62 ± 0.07 mM (ProRoot) and 1.51 ± 0.11 mM (Angelus); Fig. 4A] (Duarte MA et al., 2003). I also confirmed that cell viability was not affected by MTA concentration (Fig. 4B).

A

Material	Ca^{2+} (mM)	pH
ProRoot MTA	1.62 ± 0.07	9.32
MTA-Angelus	1.51 ± 0.11	9.28
HEPES	1	7.4

B

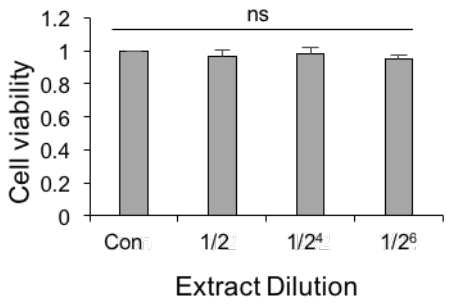

Figure 4. Ca^{2+} concentration and pH value of MTA.

(A) Ca^{2+} concentration and pH value of HEPES buffer and HEPES buffer containing calcium silicate-based biomaterials. Data are represented as mean ± SEM. (B) Viability of hDPCs at 24 hr after treatment with diluted solutions of MTA (n = 6). Data are represented as mean ± SEM. Statistical analysis was performed using a one-way ANOVA, and differences are not statistically significant.

The Effect of MTA on intracellular Ca^{2+} ($[Ca^{2+}]_i$) in hDPCs

Hydrated MTA constantly releases calcium and hydroxide ions, resulting in drastic changes in the extracellular ionic environment that is quite distinct from the intracellular environment. Based on this biochemical property of MTA, I investigated whether the intracellular Ca^{2+} level ($[Ca^{2+}]_i$) is affected by the extracellular Ca^{2+} released from hydrated MTA. To investigate the effect of MTA on $[Ca^{2+}]_i$, I transfected R-GECO1, an intensiometric genetically encoded Ca^{2+} biosensor (Zhao et al., 2011), into hDPCs and monitored the $[Ca^{2+}]_i$ changes upon MTA treatment through live cell imaging. After MTA treatment, the fluorescence intensity of R-GECO1 increased rapidly by 250%, reaching a plateau within 3 minutes in most cells [maximal half time (T1/2) = 90.00 ± 10.24 s]. In contrast, the control treatment with serum-free medium lacking MTA did not affect the fluorescence intensity of R-GECO1 (Fig. 5A and B)

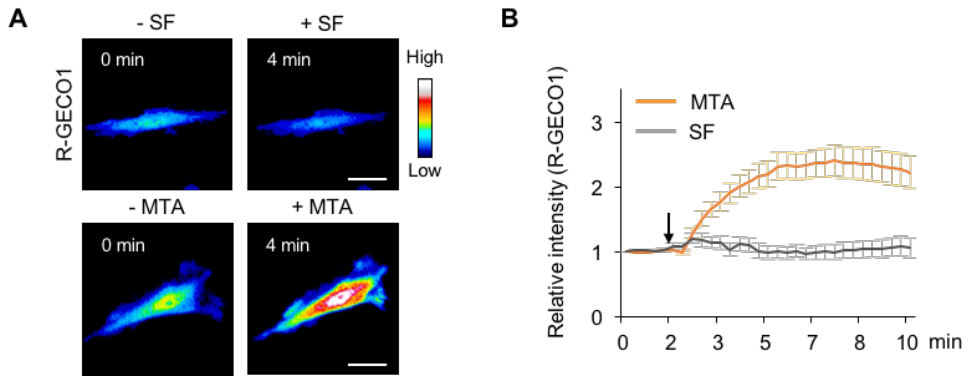

Figure 5. MTA increase intracellular Ca^{2+} $[Ca^{2+}]_i$ in hDPCs.

(A) Pseudo-colored fluorescence images of human dental pulp cells (hDPCs) expressing the Ca^{2+} biosensor R-GECO1 before (*left*) and after (*right*) treatment with serum-free media (SF) or MTA. (B) Time-dependent relative intensities of R-GECO1 in cells treated with SF (gray, n = 15) and MTA (yellow, n = 32). Arrow denotes time points of MTA treatment. Data are represented as mean ± SEM.

Identifying the origin of MTA-induced intracellular Ca^{2+} mobilization

Based on the results, I hypothesized that the increase in $[Ca^{2+}]_i$ is mediated by an influx of MTA-derived Ca^{2+}. To test this hypothesis, I pretreated hDPCs with $LaCl_3$ (a general Ca^{2+} channel inhibitor) and monitored the changes of $[Ca^{2+}]_i$ upon MTA treatment. $LaCl_3$ preincubation slightly blocked the $[Ca^{2+}]_i$ increase induced by MTA treatment, but this effect was not significant (Fig. 6A and B). The MTA-induced $[Ca^{2+}]_i$ elevation was also resistant to treatment with various Ca^{2+} channel antagonists, including SKF 96365 (calcium release-activated Ca^{2+} channels), streptomycin (stretch-activated Ca^{2+} channels), and nifedipine (L-type voltage-dependent Ca^{2+} channels), indicating that Ca^2 influx did not contribute to the observed $[Ca^{2+}]_i$ increase (Fig. 6C).

The finding that Ca^{2+} channel antagonists did not affect the MTA-induced $[Ca^{2+}]_i$ elevation paradoxically suggested that the increased $[Ca^{2+}]_i$ was intracellular in origin. To test this, I preincubated hDPCs with thapsigargin (Tg, a sarco/endoplasmic reticulum Ca^{2+}-ATPase inhibitor) to deplete Ca^{2+} in the endoplasmic reticulum (ER) before MTA treatment. Surprisingly, Tg pretreatment almost completely abolished the MTA-induced $[Ca^{2+}]_i$ increase ($P < 0.001$) (Fig. 6A and B). To further verify the Ca^{2+} mobilization from the ER upon MTA treatment, I co-utilized an ER-labeling fluorescent dye (ER-tracker) and a membrane-tethered Ca^{2+} biosensor, GCaMP6s-CAAX (Chen et

al., 2013; Tsai et al., 2014), which enables accurate detection of intracellular Ca^{2+} geometry (Kim et al., 2016). I observed that the Ca^{2+} concentration in hDPCs was initially increased from the external margin of the ER and then propagated into the cytoplasm, with sustained elevated Ca^{2+} level (Fig. 6D). Collectively, these data clearly demonstrate that the increase of $[Ca^{2+}]_i$ after MTA treatment is mainly due to the intracellular release of Ca^{2+} from the ER.

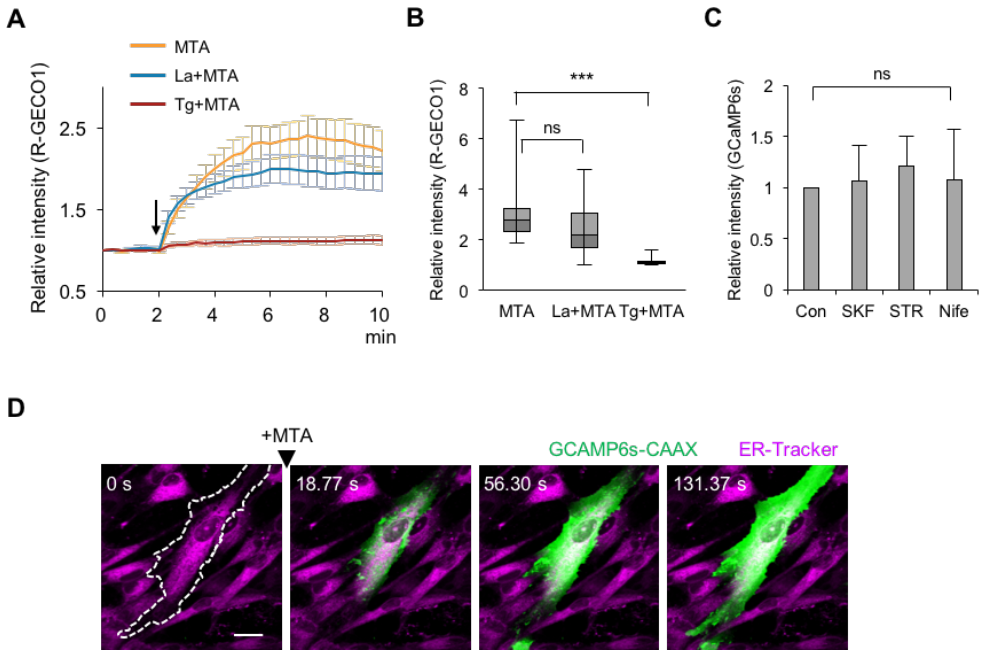
A
MTA
La+MTA
Tg+MTA
Relative intensity (R-GECO1)
2.5
1.5
0.5
0
2
4
6
8
10
min
B
Relative intensity (R-GECO1)
***
ns
8
6
4
2
0
MTA
La+MTA
Tg+MTA
C
Relative intensity (GCaMP6s)
ns
2
1.5
1
0.5
0
Con
SKF
STR
Nife
D
+MTA
GCAMP6s-CAAX
ER-Tracker
0 s
18.77 s
56.30 s
131.37 s

Figure 6. MTA-induced intracellular Ca^{2+} mobilization from ER.

(A) Time-dependent relative intensities of R-GECO1 in cells without pretreatment (yellow, n = 10) or with pretreatment of 10 μM $LaCl_3$ (blue, n = 18) and 1 μM thapsigargin (Tg) (red, n = 16), followed by MTA treatment. Arrow denotes time points of MTA treatment. Data are represented as mean ± SEM. (B) Quantification of the maximal peak intensities in panel A. Data are represented as median ± max/min. Statistical analysis was performed using the two-tailed t-test. $^{***}P<0.001$. (C) Relative intensity of GCaMP6s in hDPCs treated with various Ca^{2+} channel inhibitors. 1 μM SKF, SKF96365 (n = 14); 100 μM STR, streptomycin (n = 16); 100 μM Nife, nifedipine (n = 16). Data are represented as mean ± SEM. Statistical analysis was performed using a one-way ANOVA, and differences are not statistically significant. (D) Merged images of GCAMP6s-CAAX (green) and ER tracker (magenta) signals after MTA treatment (arrowhead).

Scale bars: 20 μm

Calcium-sensing receptor (CaSR) identification in hDPCs

Calcium-sensing receptor (CaSR), which is a member of the G protein-coupled receptor family, is a crucial mediator that links extracellular Ca^{2+} to diverse intracellular signaling cascades (Brown et al., 1993). Activated CaSR induces intracellular Ca^{2+} release from the ER through the PLC/inositol 1,4,5-triphosphate (IP_3) pathway in concert with other G protein-mediated signaling pathways (Handlogten et al., 2001) (Fig. 2). Given this information, together with the observed changes of $[Ca^{2+}]_i$ upon MTA treatment (Fig. 5A and B), I hypothesized that CaSR is the molecular sensor for MTA. According to this hypothesis, the extracellular Ca^{2+} released by MTA activates CaSR, resulting in intracellular Ca^{2+} mobilization. I first confirmed the expression of CaSR in hDPCs on both the mRNA and protein levels. Using RT-PCR, CaSR expression was detected in both hDPCs and Jurkat cells, the latter of which is a human T-lymphocyte cell line used as a positive control (Li et al., 2013) (Fig. 7A). Immunostaining analysis also revealed clear CaSR signals in the ER as well as on the plasma membrane, indicating a dynamic trafficking-recycling process of CaSR in hDPCs (Fig. 7B).

To characterize the expression pattern of CaSR in hDPCs more clearly, I investigated subcellular localization of CaSR in cells stained with anti-CaSR, anti-plasma membrane Ca^{2+} ATPase (PMCA; used as a membrane marker),

an ER-tracker and anti-GM-130 (used as a golgi marker) through high-magnification confocal microscopy (>40× objective). I was able to determine the expression pattern of CaSR on ER and the plasma membrane, where it was co-localized with the PMCA signal (Fig. 8). In particular, CaSR expression was clearly seen on the membrane ruffled border (Fig. 8, arrowheads), indicating functional expression of the membrane receptor. CaSR was not expressed in golgi, where it was not co-localized with GM-130 signal (Fig. 8).

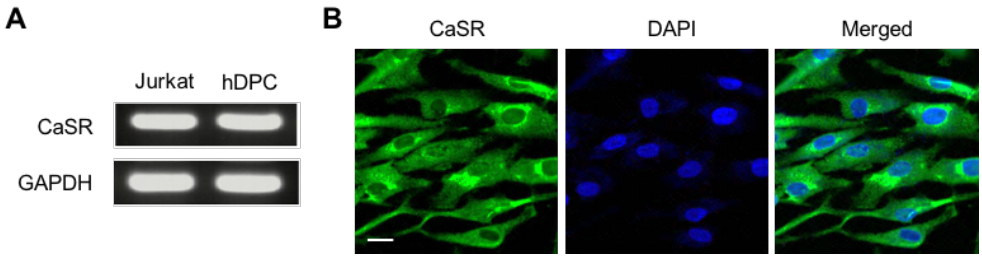

Figure 7. Expression of CaSR in hDPCs.

(A) mRNA expression levels of CaSR in Jurkat cells and hDPCs. (B) Immunofluorescence images of CaSR (green) and DAPI (blue) in hDPCs.

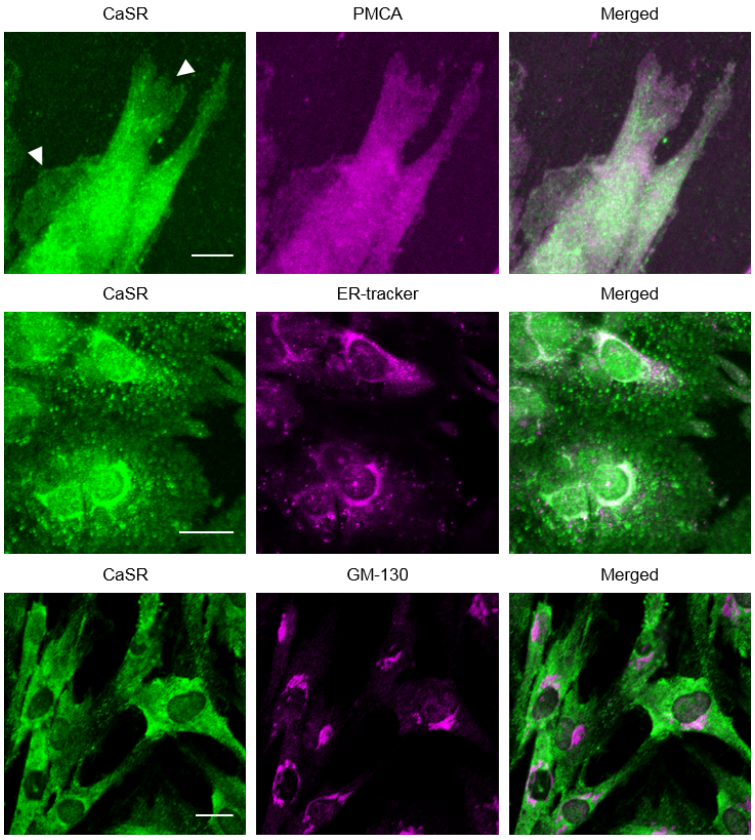

Figure 8. Intracellular localization of CaSR in hDPCs.

Cells were stained with anti-CaSR (green), anti-plasma membrane Ca^{2+} ATPase (PMCA, magenta) as the membrane marker, an ER-tracker (magenta), and anti-GM-130 (magenta) as a Golgi marker. A merged image of two channels is shown on the right panel.

Scale bars: 20 μm.

CaSR is a crucial mediator of MTA-mediated intracellular signaling pathway

Next, I found that the MTA-induced $[Ca^{2+}]_i$ increase was significantly inhibited when cells were pretreated with a specific CaSR antagonist, NPS2143 ($P < 0.001$; Fig. 9A and B). Moreover, pretreatment with U73122 (a PLC inhibitor) clearly attenuated the amplitude of the $[Ca^{2+}]_i$ increase induced by MTA treatment [peak increase: 25.44 ± 3.40% (control); 5.15 ± 2.77% (U73122); Fig. 10A and B]. These results indicate that the CaSR-PLC signaling axis is crucial for MTA-induced intracellular Ca^{2+} mobilization.

I next investigated whether MTA activates other downstream signaling pathways induced by CaSR. I performed live-cell imaging of hDPCs expressing a phosphatidyl inositol-3 phosphate (PIP_3) biosensor (dTomato-PH_{AKT1}; Fig. 11A) (Kim et al., 2014) to investigate the effect on phosphoinositide 3-kinase (PI3K) activity. After MTA treatment, the dTomato-PH_{AKT1} cytoplasmic signal was remarkably decreased (-74.32 ± 0.05% compared with the basal level) due to its translocation to the plasma membrane (Fig. 11A and B). Under the same conditions, there was no change in the dTomato-PH_{AKT1} cytoplasmic signal with preincubation of NPS2143 (Fig. 11B). I also confirmed the involvement of the MAPK pathway in CaSR downstream signaling by analyzing ERK phosphorylation upon MTA

treatment and combinatorial treatment with NPS2143 via immunoblotting (Fig. 11C). MTA induced phosphorylation of ERK, while treatment with NPS 2143 reduced MTA-induced ERK phosphorylation (Fig. 11C). Taken together, these data suggest that MTA activates diverse canonical downstream pathways of CaSR.

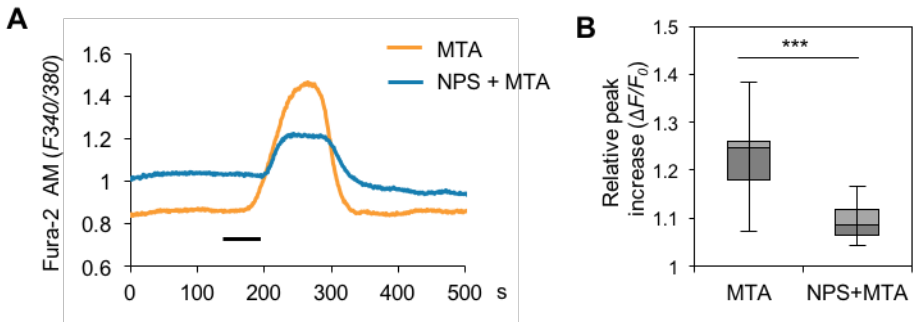

Figure 9. NPS2143 inhibits MTA-induced $[Ca^{2+}]_i$ increase.

(A) Trace of Fura-2 fluorescence (F/F_0) change upon MTA addition, with or without NPS2143 treatment. (B) Measured relative peak increase in panel A. n = 12 (MTA); n = 13 (NPS + MTA). Data are represented as median ± max/min. Statistical analysis was performed using the two-tailed t-test. $^{***}P<0.001$.

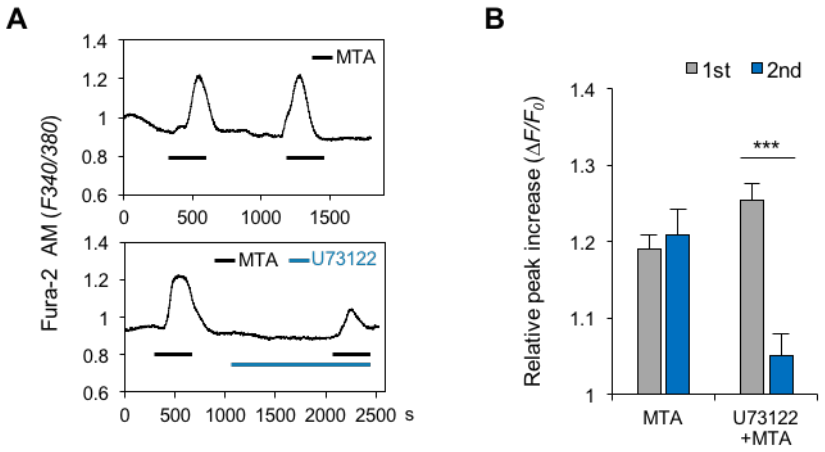

Figure 10. U73122 inhibits MTA-induced $[Ca^{2+}]_i$ increase.

(A) Trace of MTA-induced Fura-2 fluorescence changes with or without 1 μM U73122 treatment. (B) Quantification of the maximal peak increases in panel D. n = 5 (MTA); n = 9 (U73122 + MTA). Data are represented as median ± max/min. Statistical analysis was performed using the two-tailed t-test. $^{***}P<0.001$.

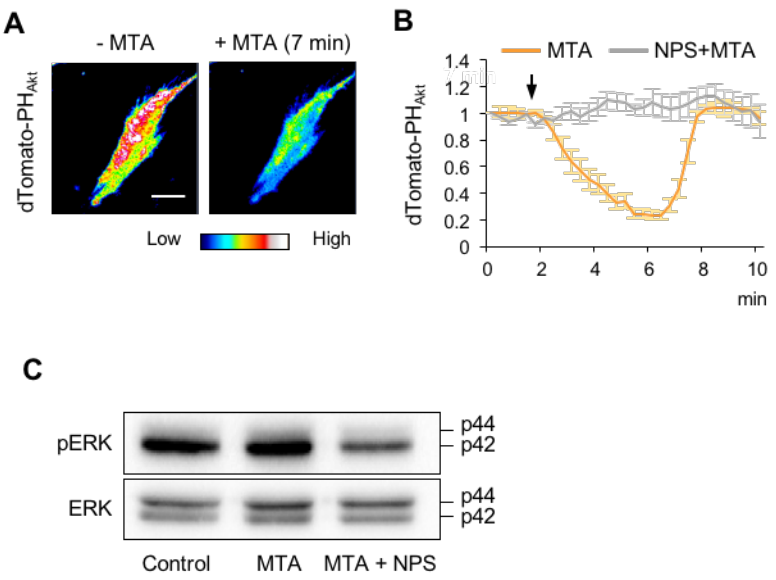

Figure 11. NPS2143 inhibits MTA-induced phosphoinositide 3-kinase (PI3K) activity and ERK phosphorylation.

(A) Pseudo-colored fluorescence images of hDPCs expressing dTomato-PH_{AKT1} (biosensor for the PI3K pathway), before (*left*) and after (*right*) MTA treatment. (B) Cytoplasmic intensities of dTomato-PH_{AKT1} in hDPCs upon MTA treatment, without (gray, $n = 12$) or with (yellow, $n = 8$) 1 μM NPS2143. Data are represented as mean ± SEM. (C) Immunoblot analysis of phosphorylated ERK (*upper*) and ERK (*lower*) upon MTA treatment, with or without NPS2143, for 24 hr.

Scale bars: 20 μm.

Distinct effects of MTA-mediated Ca^{2+} and pH modulation on CaSR signaling dynamics

Next, I investigated the relationship between environmental chemistry (which is altered by MTA application) and CaSR signaling activity. To investigate the individual effects of MTA-induced Ca^{2+} and alkaline pH on CaSR signaling activity, I mimicked each ionic condition of MTA by modifying the ionic concentrations of normal HEPES buffer (1 mM Ca^{2+} with pH 7.4). Specifically, I generated two modified HEPES buffers, one with an altered Ca^{2+} concentration (HEPESΔCa^{2+}: 2 mM Ca^{2+} with pH 7.4) and the other with altered pH (HEPESΔpH: 1 mM Ca^{2+} with pH 9), by adding $CaCl_2$ and NaOH, respectively (Fig. 12A). Using a Fura-2 ratiometric imaging system, I found that the HEPESΔpH buffer increased the $[Ca^{2+}]_i$ of hDPCs by a similar amount and in a similar time frame as the MTA solution, while the HEPESΔCa^{2+} buffer resulted in a subtle change of $[Ca^{2+}]_i$ level [peak increase: 63.53 ± 6.72% (MTA), 48.68 ± 6.21% (HEPESΔpH), 7.13 ± 1.64% (HEPESΔCa^{2+}); Fig. 12B]. To further verify the contribution of each factor to CaSR activity, I mornitored $[Ca^{2+}]_i$ level upon changes of extracellular Ca^{2+} concentration ($[Ca^{2+}]_e$, ranging from 0 to 5 mM) and pH (pH_e, 7.4 and 9.4). Intracellular Ca^{2+} mobilization was detected from 1 mM $[Ca^{2+}]_e$, and the amplitude of the

mobilization was increased according to the $[Ca^{2+}]_e$ enhancement (Fig. 12C). Intriguingly, alkaline pH remarkably increased the amplitude in all cases of $[Ca^{2+}]_e$, except in the absence of extracellular Ca^{2+} (Fig. 12C), indicating that extracellular Ca^{2+} and alkaline pH synergistically activate CaSR.

Moreover, the MTA solution with neutral pH (HCl-adjusted) showed significantly reduced signaling activity compared to the prototype MTA solution ($P < 0.001$; Fig. 13A and B).

The pH-induced $[Ca^{2+}]_i$ rise was clearly inhibited by NPS2143 treatment [peak increase: 48.77 ± 5.41% (HEPESΔpH), 10.03 ± 1.57% (HEPESΔpH + NPS2143); $P < 0.01$; Fig. 14A and B]. These data imply that alkaline pH resulting from MTA exposure plays an important role in the overall Ca^{2+} response induced by CaSR activation.

I additionally confirmed that $[Ca^{2+}]_i$ was not altered by the sodium and chloride ions that are added during the pH adjustment of the experimental solutions (Fig. 15A). Moreover, due to the possibility that pH could be altered by $[Ca^{2+}]_i$ changes (Hwang et al., 2011), I confirmed that intracellular pH was not affected by MTA treatment (Fig. 15B).

A

	Ca^{2+} (mM)	pH
MTA	2	9
HEPES ΔCa^{2+}	2	7
HEPES ΔpH	1	9
HEPES	1	7

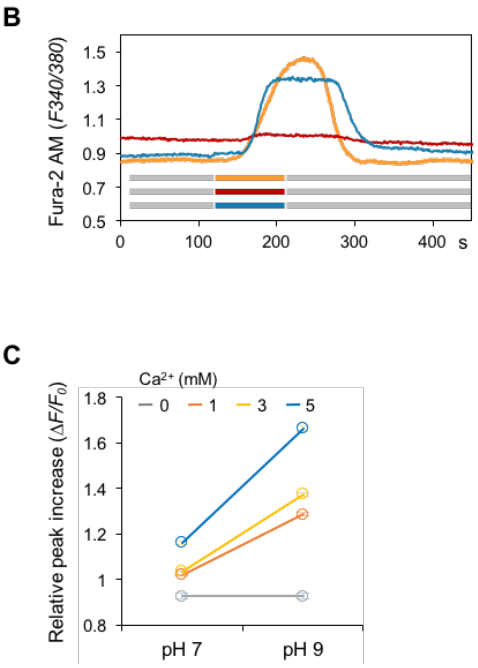

Figure 12. The individual effects of Ca^{2+} and alkaline pH release from MTA on $[Ca^{2+}]_i$ response.

(A) Ca^{2+} concentration and pH of MTA and modified HEPES buffers. (B)Trace of Fura-2 fluorescence after treatment with MTA or modified HEPES buffers. (C) Measured relative peak increase of Fura-2 fluorescence from 0 to 5 mM $[Ca^{2+}]_e$ at pH_e 7.4 and 9.4. $n > 10$. Data are represented as mean ± SEM.

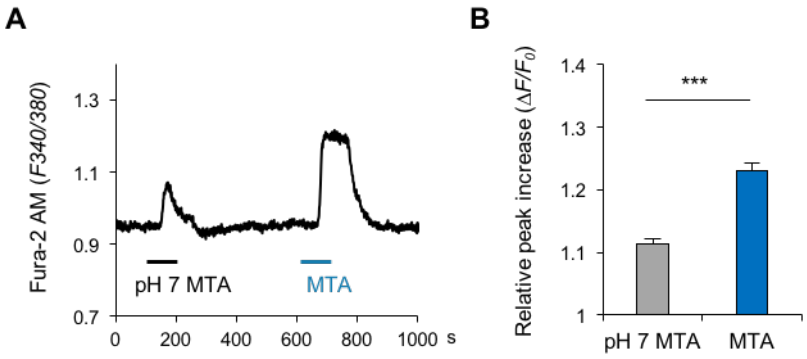

Figure 13. Neutral pH of MTA is significantly reduced $[Ca^{2+}]_i$ response.

(A) Trace of Fura-2 fluorescence measured with neutralized MTA (pH 7) and prototype MTA treatment. (B) Quantification of the maximal peak increases in panel D. n = 22. Data are represented as mean ± SEM. Statistical analysis was performed using the two-tailed t-test. $^{***}P<0.001$.

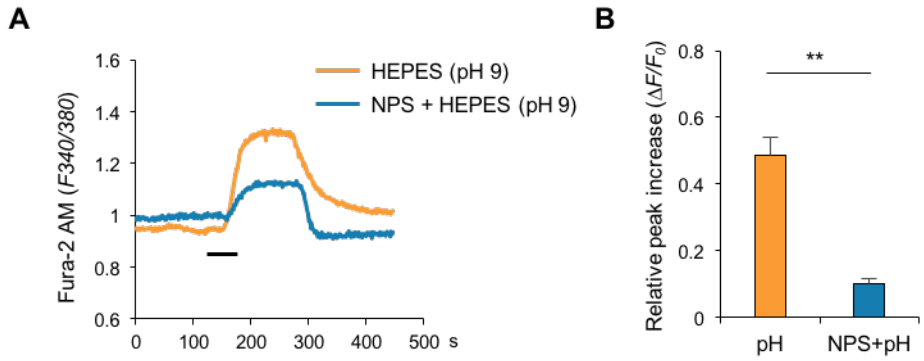

Figure 14. NPS2143 inhibits alkaline pH-induced $[Ca^{2+}]_i$ increase.

(A) Trace of HEPES (pH 9)-induced Fura-2 fluorescence, measured with or without NPS 2143 treatment. (B) Peak increase from panel A. $n = 12$ (HEPES pH 9); $n = 9$ (NPS 2143 + HEPES pH 9). Data are expressed as mean ± SEM. Statistical analysis was performed using the two-tailed t-test. $^{**}P<0.01$.

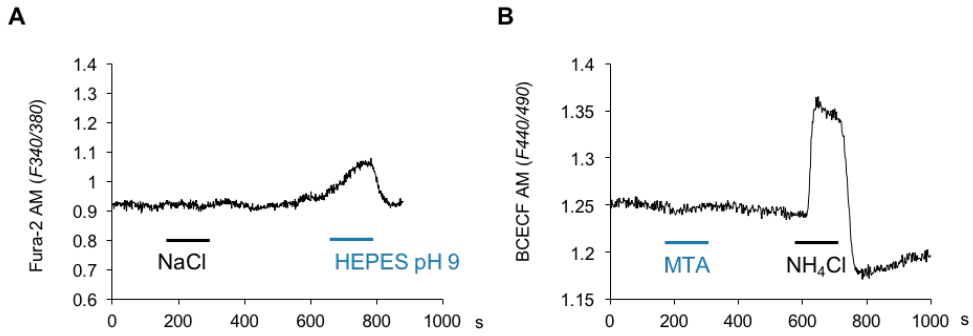

Figure 15. $[Ca^{2+}]_i$ and pH_i was not affected by experimental solutions.

(A) Effect of sodium chloride on $[Ca^{2+}]_i$ level. The same concentration of sodium ion was used as Fig14 for the pH adjustment of HEPES. (B) Effect of MTA on intracellular pH (pH_i) in hDPCs upon MTA treatment. NH_4Cl was used as a positive control.

Effect of pH_e alteration on CaSR signaling kinetics

Next, I analyzed the effect of pH_e alteration on CaSR signaling dynamics. To this end, I collected $[Ca^{2+}]_i$ kinetic data while changing the pH_e from 6.4 to 11.4 in the presence of 1 mM $[Ca^{2+}]_e$ (Fig. 16A). The maximal amplitude and activation/deactivation kinetics of the signals are presented as value of peak increase ($\Delta F/F_0$) and half-maximal time of activation/deactivation ($T1/2_{act}$ and $T1/2_{deact}$), respectively. The peak increase of $[Ca^{2+}]_i$ tended to increase as pH_e increased from 6.4, with maximal amplitude at around pH_e 10.4 (Fig. 16B). I also found that pH_e modulates signaling kinetics through half-maximal time analysis. Specifically, when the pH_e became alkaline, the activation kinetics of $[Ca^{2+}]_i$ became faster (decreased $T1/2_{act}$) and showed sustained signaling patterns (increased $T1/2_{deact}$; Fig. 16C). These data indicate that MTA-induced Ca^{2+} and alkaline pH play distinct roles in CaSR activation. Specifically, Ca^{2+} acts as a crucial ligand for turning on CaSR, whereas pH regulates CaSR signaling dynamics in a versatile manner (Fig. 22).

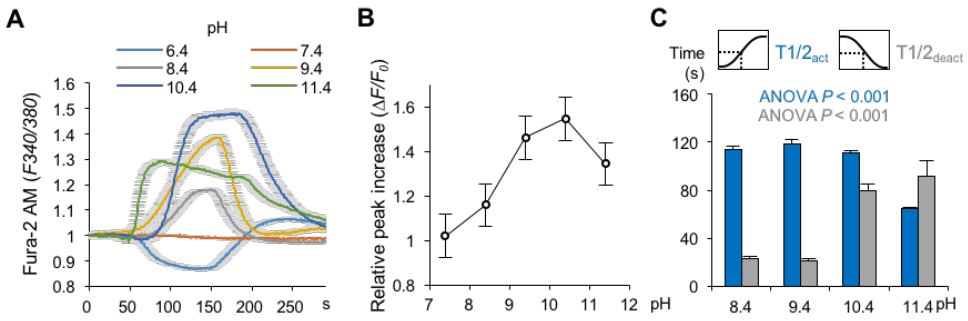

Figure 16. Kinetics of pH_e alteration in hDPCs.

(A) Changes in Ca^{2+} signaling kinetics upon pH_e alteration in 1 mM $[Ca^{2+}]_e$. (B) Relative peak increase of Fura-2 fluorescence upon pH_e alteration. (C) Quantification of the maximal half time of activation (blue, $T1/2_{act}$) and deactivation (gray, $T1/2_{deact}$) kinetics upon pH_e alteration. $n > 15$. Data are represented as mean ± SEM.

Effect of MTA on NFAT activity

I finally tested the effect of MTA on cellular function and the involvement of CaSR in this response. The effects of MTA on odonto/osteogenic differentiation have been reported in various cell types (Maeda et al., 2010; Yan et al., 2014; Yasuda et al., 2008), but the relevant intracellular signaling pathway remains to be elucidated. Therefore, I hypothesized that intracellular Ca^{2+} mobilization by CaSR activation changes gene expression patterns during the differentiation process (Fig. 17). To test this hypothesis, I investigated the activity of nuclear factor of activated T cells (NFAT), a Ca^{2+}-dependent transcription factor (Hogan et al., 2003), by monitoring translocation of a fluorescent protein-tagged NFATc1 (mCherry-NFAT) following MTA treatment. In serum-starved hDPCs, the mCherry-NFAT signal was predominantly localized in the cytoplasm [62.86 ± 4.28% (cytoplasm) versus 37.14 ± 4.28% (nucleus)]. After treatment with MTA, NFAT-mCherry was robustly translocated into the nucleus [30.73 ± 1.84% (cytoplasm) versus 69.26 ± 1.84% (nucleus)]; this activity was sustained (Fig. 18A and B).

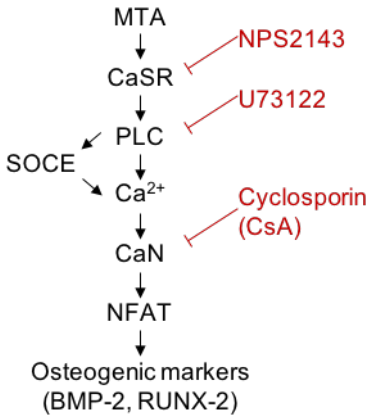

Figure 17. Suggested pathway of MTA-induced osteoblast differentiation.

Experimental design for inhibiting signaling nodes in the CaSR-NFAT signaling cascade. SOCE, store operated Ca^{2+} entry; CaN, calcineurin; nuclear factor of activated T cells (NFAT)

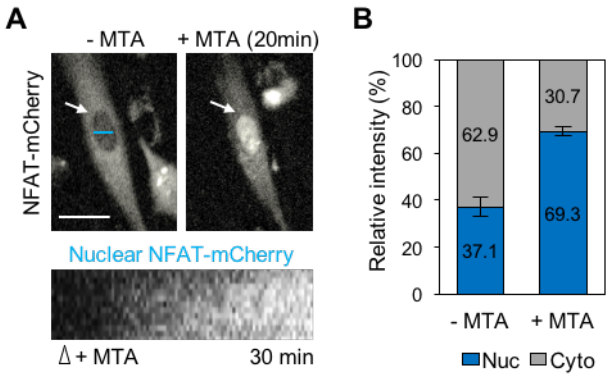

Figure 18. MTA activated nuclear factor of activated T cells (NFAT) translocation.

(A) *Upper panel*: Pseudo-colored fluorescence images of hDPCs expressing NFATc1-mCherry before (*left*) and after (*right*) MTA treatment. *Lower panel*: Pseudo-colored line-scanned image (kymograph) of the nuclear NFAT-mCherry signal. White arrows indicate the nucleus. The blue line indicates the line-scanned region. The white arrow head indicates the time point of MTA treatment. (B) Relative distribution of NFAT-mCherry intensity between the nucleus (Nuc, blue) and the cytoplasm (Cyto, gray) of hDPCs before and after MTA treatment. $n = 7$. Data are represented as mean ± SEM.

Scale bars: 50 μm.

Involvement of CaSR-NFAT signaling cascade on MTA-induced osteogenic differentiation

I next investigated whether osteogenic differentiation of hDPCs is mediated by the CaSR-to-NFAT signaling cascade. I then conducted real-time PCR to quantify the mRNA levels of bone morphogenic protein (BMP)-2 and Runt-related transcription factor 2 (RUNX2), two representative osteogenic differentiation markers, after treatment with MTA, and with inhibitors of upstream signaling components of NFAT (Fig. 19). BMP-2 and RUNX2 mRNA levels were upregulated in hDPCs 12 and 24h after MTA treatment, and these effects were clearly blocked by CaSR, PLC and calcineurin inhibitors [NPS2143, U73122, and cyclosporin A (CsA), respectively; Fig. 19A and B]. Immunofluorescence analysis revealed that MTA-treated cells showed increased BMP-2 signal (Fig. 19C), whereas this upregulated expression was significantly blocked by cotreatment with NPS2143, U73122, and CsA (Fig. 19D). I also demonstrated the long-term effect (up to 21 days) of CaSR pathway in the genetic changes by MTA through analyzing the expression profiles of diverse osteogenic/odontogenic markers (Fig. 20). BMP-2 and DSPP were increased in early stages of differentiation (day 7), and RUNX2, OPN, and COL3A1 showed robust up-regulation at day 14 (Fig. 20).

Importantly, CaSR selective inhibitor, NPS 2143, efficiently blocked the increasing effect of MTA on the gene expression (Fig. 20). Unfortunately, MTA did not enhance the expression of OCN and DMP1 in our experimental condition.

Finally, the actual mineralization potential of hDPCs was evaluated by alizarin red S staining and alkaline phosphatase (ALP) activity measurement. The results revealed a significant increase in mineralization when cells were exposed to MTA for 21 days compared with exposure to differentiation media only. As expected, a remarkable attenuation in stained matrices was observed in cells treated with NPS 2143 or U73122 (Fig. 21A). Also, hDPCs with NPS 2143 or U73122 treatment had a lower ALP activity than the MTA treatment cells (Fig. 21B). In summary, the CaSR-PLC-Ca^{2+}-NFAT signaling axis is a crucial mediator of MTA-induced osteogenic differentiation of hDPCs (Fig. 22).

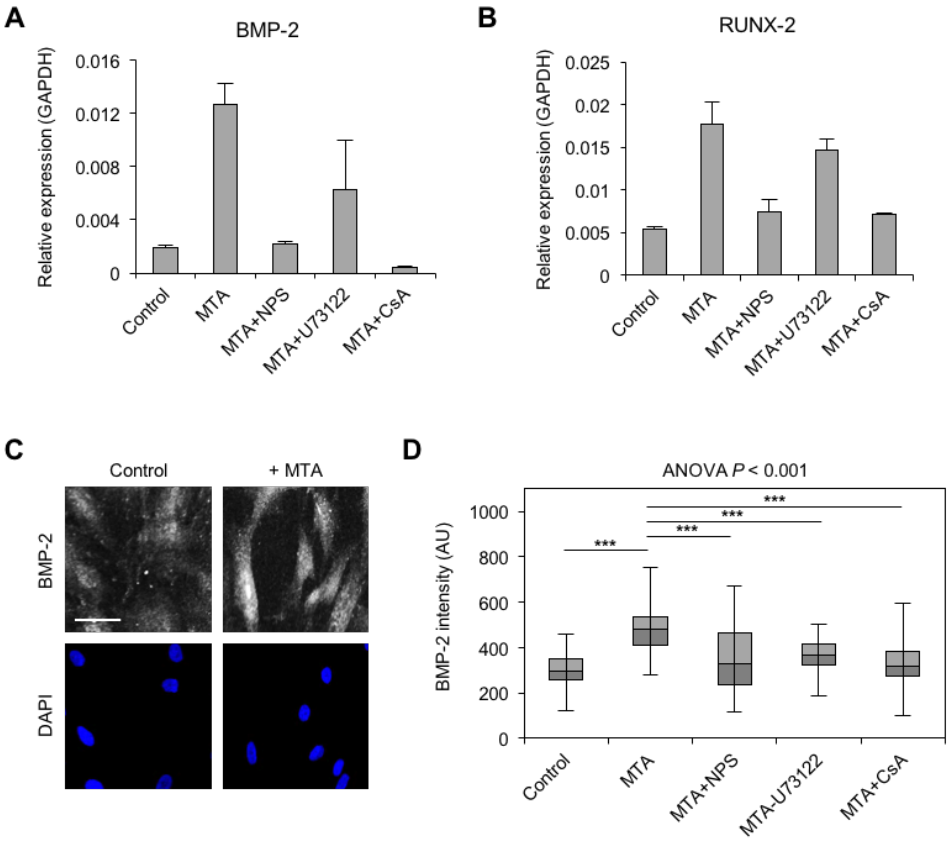
A
BMP-2
Relative expression (GAPDH)
0.016
0.012
0.008
0.004
0
Control
MTA
MTA+NPS
MTA+U73122
MTA+CsA
B
RUNX-2
Relative expression (GAPDH)
0.025
0.02
0.015
0.01
0.005
0
Control
MTA
MTA+NPS
MTA+U73122
MTA+CsA
C
Control
+ MTA
BMP-2
DAPI
D
ANOVA P < 0.001
BMP-2 intensity (AU)
1000
800
600
400
200
0
***
***
***
***
Control
MTA
MTA+NPS
MTA-U73122
MTA+CsA

Figure 19. Expression patterns of osteoblastic makers during inhibition of CaSR-NFAT signaling cascade.

(A and B) mRNA expression of osteogenic markers (BMP-2 and RUNX2) after treatment with inhibitors of CaSR downstream pathways. Cells were incubated with the reagents for 12 hr (BMP-2) or 24 hr (RUNX2). Data are represented as mean ± SEM. (C) Representative immunofluorescence images of BMP-2 (gray) and DAPI (blue) in hDPCs. (D) Immunofluorescence intensity of BMP-2 in hDPCs after treatment with inhibitors of CaSR downstream pathways. AU: arbitrary unit, n = 40. Data are represented as median ± max/min. *** $P < 0.001$.

Scale bars: 50 μm.

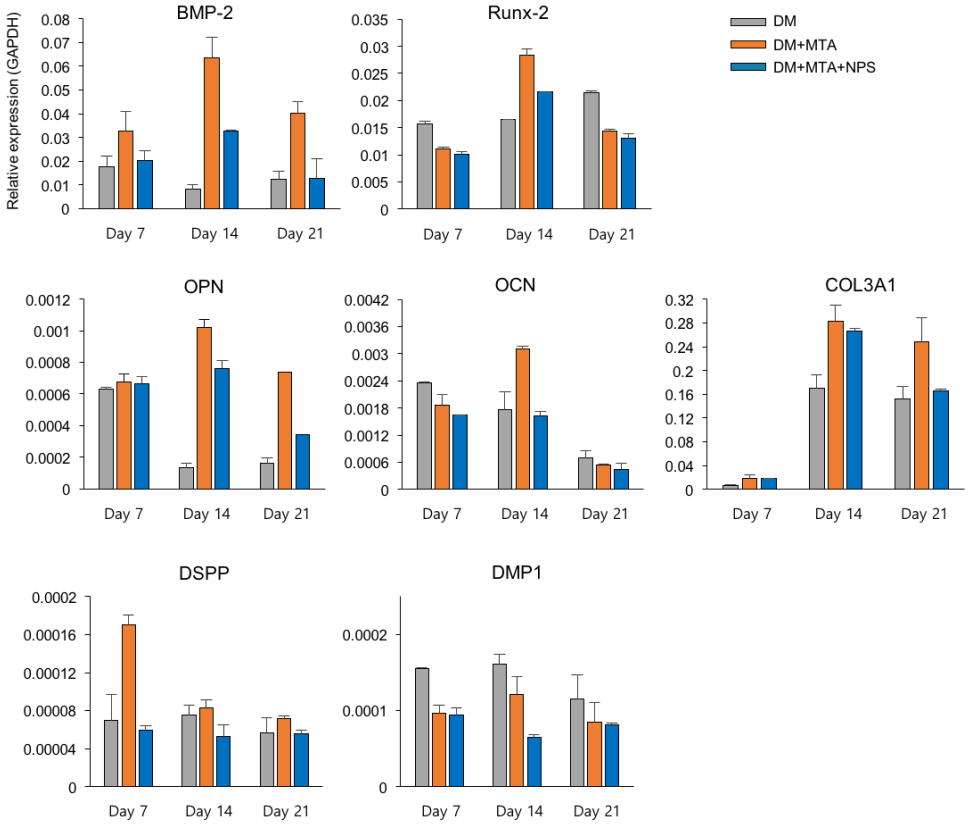
BMP-2
Runx-2
OPN
OCN
COL3A1
DSPP
DMP1
Relative expression (GAPDH)
DM
DM+MTA
DM+MTA+NPS
Day 7
Day 14
Day 21

Figure 20. Expression patterns of osteogenic/odontogenic markers during differentiation.

Expression profiles of osteogenic/odontogenic markers in hDPCs cultured in differentiation media (DM; gray), differentiation media containing MTA (orange), or MTA with NPS 2143 (blue) for 7, 14, and 21 days. BMP-2: bone morphogenic protein 2; RUNX2: runt-related transcription factor 2; OPN: osteopontin; OCN: osteocalcin; COL3A1: collagen type III alpha 1 chain; DSPP: dentin sialophosphoprotein; DMP1: dentin matrix acidic phosphoprotein 1. Data are presented as mean ± SEM.

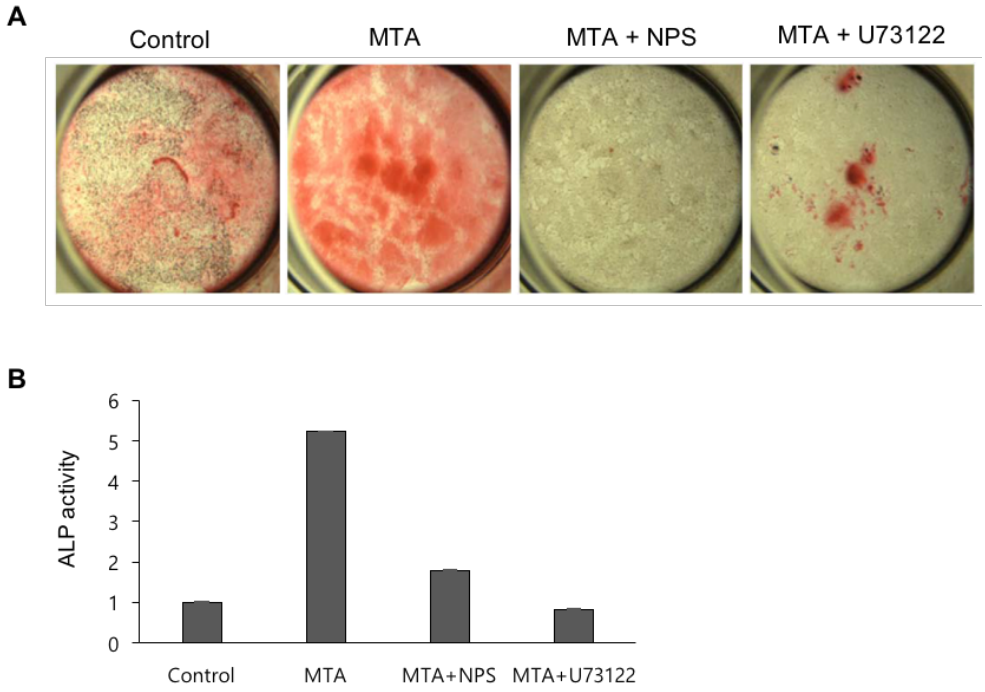

Figure 21. CaSR-NFAT signaling cascade regulates MTA-induced mineralization.

(A) Alizarin red S staining results of hDPCs in differential media, differential media containing MTA, and with inhibitors of CaSR downstream pathways. (B) Relative activity of alkaline phosphatase (ALP) of hDPCs in differential media, differential media containing MTA, and with inhibitors of CaSR downstream pathways.

Discussion

Since the development of MTA, a number of biological studies have focused on the biocompatibility of MTA or the functional readouts of cells and tissue after MTA treatment. Despite of such long-term application, the molecular mechanism of MTA is still largely unknown, unfortunately. Although calcium silicate-based biomaterials represented by MTA have been identified as essential materials in pulp and periodontal regeneration, the molecular mechanism of these materials is relatively poorly understood compared to other physiological ligands used for regenerative treatment, such as fibroblast growth factor (FGF) and transforming growth factor-β (TGF-β). The critical point is the fact that MTA is a chemical compound (mixture of calcium silicate derivatives), not a pure material. The insufficient scientific background about complex MTA biochemistry could bring out potential toxicity or unwanted consequence due to the unknown chemical reaction or ingredients of MTA. Meanwhile, a number of researchers have been tried to improve MTA's biological effect and physical properties by combinatorial treatment with other reagent and just 'mixing' it with restorative materials (e.g., resin, glass ionomer), respectively. However, without molecular basis of MTA, these

trials can be a great tragedy, and also are not in coincidence with the concept of evidence-based therapy. In terms of evidence-based therapy, this insufficient understanding of the mechanism of bioactive materials restricts their relevant use in clinical situations as well as their application to new therapeutic modalities (e.g., combination therapy). Therefore, throughout this study, I sought to construct an overall blueprint of the intracellular signaling mechanism that mediates MTA-induced biological reactions.

In this work, I demonstrated that MTA-induced extracellular changes of Ca^{2+} and pH synergistically activate CaSR. I showed that CaSR translates the signaling input from MTA into diverse downstream pathways in hDPCs and also demonstrated that the CaSR-mediated $[Ca^{2+}]_i$ increase plays an important role in the osteogenic differentiation of hDPCs. Based on these data, I propose a model based on the CaSR signaling cascade to explain the mechanism of MTA (Fig. 22). CaSR expression was first reported in the parathyroid glands, which regulate parathyroid hormone release by sensing the serum Ca^{2+} concentration (Brown et al., 1993). CaSR expression and functions has also been reported in diverse organs involved in maintaining Ca^{2+} homeostasis, both directly and indirectly, including the kidney, breast, nervous system, and bone (Magno et al., 2011). Especially, CaSR has been known to regulate bone remodeling; CaSR activation induced osteoblast proliferation (Dvorak et al.,

2004), and CaSR knock-out mice exhibited undermineralization phenotypes in developing skeletal system (Chang et al., 2008; Sun et al., 2010). These critical roles of CaSR in the mineralization process strengthen our finding that CaSR is a potent mediator in MTA-induced regeneration of the pulp-dentin complex and alveolar bone. However, the role of CaSR in a dental field is just beginning to be understood. I expect that achieving a better understanding of CaSR-mediated downstream signaling will provide core information for improving and developing the existing and next materials in regenerative dentistry.

By quantitating the $[Ca^{2+}]_i$ changes under different pH and Ca^{2+} concentrations (Fig. 11C), I identified distinct roles of Ca^{2+} and alkaline pH of MTA in CaSR signaling activity. I also found that Ca^{2+} ions released from MTA activate CaSR, and that the resultant Ca^{2+} mobilization from the ER is a key signal in MTA-induced biological reactions. However, several Ca^{2+} channels have also been suggested as possible mediators of Ca^{2+}-releasing materials such as calcium hydroxide or MTA (Kimura et al., 2016; Sohn et al., 2015; Tada et al., 2010). The presence of Ca^{2+} influx through the channels was demonstrated by the residual intracellular Ca^{2+} signals that were observed after MTA treatment with CaSR and PLC inhibitors (Fig. 9A and B). I propose that this Ca^{2+} influx acts as a supporting signal for regulating $[Ca^{2+}]_i$ level, most

likely affecting the amplitude or duration of the signaling. For instance, the Ca^{2+} release-activated Ca^{2+} (CRAC) channel Orai1, which plays a significant role in MTA-induced odontogenic differentiation (Sohn et al., 2015), sustains the $[Ca^{2+}]_i$ level via store-operated Ca^{2+} entry after PLCγ activation, thus increasing NFAT transcriptional activity (Feske et al., 2006).

Interestingly, a wide variety of CaSR signaling properties (e.g., activation/deactivation kinetics and amplitude) were fine-tuned upon the alteration of extracellular pH, rather than of Ca^{2+} concentration (Fig. 16A-C). I found that maximal signaling activity was elicited in the alkaline pH range 10 to 11 (≈ 10.4; Fig. 16B), which corresponds to the optimum pH for maximal mineralization (represented by alkaline phosphatase activity) (Heithersay, 1975). These findings support the possibility that extracellular pH is a dominant factor in modulating CaSR-mediated mineralization. If so, how does extracellular pH modulate CaSR activity? A previous study reported that alkaline pH increased the agonist sensitivity of CaSR, and that an acidic condition had the reverse effect (Quinn et al., 2004), but the molecular mechanism underlying these effects was not investigated. One possible interpretation is that pH alteration induces variations in the net electrical charges of CaSR agonists or the charged residues in the extracellular domains

of the receptors, thereby changing the receptor conformations via allosteric modulation (Quinn et al., 2004). The pH-dependent diversity of CaSR activity might be closely related to the clinical efficacy of MTA in specific pathological conditions such as inflammation, in which the acidic environment associated with chronic inflammation can mitigate the biological activity of MTA. Therefore, the ability to maintain the alkaline pH of calcium silicate-based materials should be carefully considered when applying or improving the biological activity of the material for diverse clinical situations.

MTA also contains other chemical components that mainly consist of diverse cations such as silicon, aluminum, iron (gray MTA), and magnesium ions (Sarkar et al., 2005), which may perturb unexpected signaling pathways. However, there is no clear evidence that these cations are released to the surrounding tissues after MTA setting. Moreover, CaSR responds to a wide range of polyvalent cations with varying efficacies, in addition to Ca^{2+} ions (Handlogten et al., 2000; Hofer and Brown, 2003). For instance, Al^{3+} was reported to be a weak agonist (mM concentrations) of CaSR (Spurney et al., 1999). This property might be due to the extracellular binding pocket of CaSR having a promiscuous affinity to diverse cations. Given these evidences, it is reasonable to regard CaSR as a core biological mediator that responds to the chemical changes induced by MTA application.

Throughout this study, I demonstrated that CaSR is a crucial signaling mediator of MTA-induced biological effects. My results clarify the molecular mechanism that links chemical reactions of MTA to its biological effects. I anticipate that these advanced understandings will provide potential evidences for developing novel biomaterials for regenerative therapies.

References

Berridge MJ, Lipp P, Bootman MD (2000). The versatility and universality of calcium signalling. Nat Rev Mol Cell Biol. 1(1):11-21.

Brown EM, Gamba G, Riccardi D, Lombardi M, Butters R, Kifor O, Sun A, Hediger MA, Lytton J, Hebert SC (1993). Cloning and characterization of an extracellular Ca^{2+}-sensing receptor from bovine parathyroid. Nature. 366(6455):575-80.

Brown EM, MacLeod RJ (2001). Extracellular calcium sensing and extracellular calcium signaling. Physiol Rev. 81(1):239-297.

Camilleri J, Montesin FE, Brady K, Sweeney R, Curtis RV, Ford TR (2005). The constitution of mineral trioxide aggregate. Dent Mater. 21(4):297-303.

Camilleri J (2007). Hydration mechanisms of mineral trioxide aggregate. Int Endod J. 40(6):462-70.

Chang W, Tu C, Chen TH, Bikle D, Shoback D (2008). The extracellular calcium-sensing receptor (CaSR) is a critical modulator of skeletal development. Sci Signal. 1(35).

Chen TW, Wardill TJ, Sun Y, Pulver SR, Renninger SL, Baohan A, Schreiter ER, Kerr RA, Orger MB, Jayaraman V, Looger LL, Svoboda K, Kim DS (2013). Ultrasensitive fluorescent proteins for imaging neuronal activity. Nature. 499(7458):295-300.

Conigrave AD, Quinn SJ, Brown EM (2000). Cooperative multi-modal sensing and therapeutic implications of the extracellular Ca^{2+}-sensing receptor. Trends Pharmacol Sci. 21(10):401-7.

Duarte MA, Demarchi AC, Yamashita JC, Kuga MC, Fraga Sde C (2003). pH and calcium ion release of 2 root-end filling materials. Oral Surg Oral Med Oral Pathol Oral Radiol Endod. 95(3):345-7.

Dvorak MM, Siddiqua A, Ward DT, Carter DH, Dallas SL, Nemeth EF, Riccardi D (2004). Physiological changes in extracellular calcium

concentration directly control osteoblast function in the absence of calciotropic hormones. Proc Natl Acad Sci U S A. 101(14):5140-5.

Feske S, Gwack Y, Prakriya M, Srikanth S, Puppel SH, Tanasa B Hogan PG, Lewis RS, Daly M, Rao A (2006). A mutation in Orai1 causes immune deficiency by abrogating CRAC channel function. Nature. 441(7090):179-85.

Fridland M, Rosado R (2005). MTA solubility: a long term study. J Endod. 31(5):376-9.

Handlogten ME, Shiraishi N, Awata H, Huang C, Miller RT (2000). Extracellular Ca^{2+}-sensing receptor is a promiscuous divalent cation sensor that responds to lead. Am J Physio Renal physiol. 279(6):F1083-91.

Handlogten ME, Huang C, Shiraishi N, Awata H, Miller RT (2001). The Ca^{2+}-sensing receptor activates cytosolic phospholipase A2 via a Gqalpha -dependent ERK-independent pathway. J Biol Chem. 276(17):13941-8.

Heithersay GS (1975). Calcium hydroxide in the treatment of pulpless teeth with associated pathology. J Br Endod Soc. 8(2):74-93.

Hofer AM, Brown EM (2003). Extracellular calcium sensing and signalling. Nat Rev Mol. 4(7):530-8.

Hogan PG, Chen L, Nardone J, Rao A (2003). Transcriptional regulation by calcium, calcineurin, and NFAT. Genes Dev. 17(18):2205-32.

Hwang SM, Koo NY, Jin M, Davies AJ, Chun GS, Choi SY, Kim JS, Park K (2011). Intracellular acidification is associated with changes in free cytosolic calcium and inhibition of action potentials in rat trigeminal ganglion. J Bio Chem. 286(3):1719-29.

Kim JM, Lee M, Kim N, Heo WD (2016). Optogenetic toolkit reveals the role of Ca^{2+} sparklets in coordinated cell migration. Proc Natl Acad of Sci U S A. 113(21):5952-7.

Kim N, Kim JM, Lee M, Kim CY, Chang KY, Heo WD (2014). Spatiotemporal control of fibroblast growth factor receptor signals by blue light. Chem Biology. 21(7):903-12.

Kimura M, Sase T, Higashikawa A, Sato M, Sato T, Tazaki M, Shibukawa Y (2016). High pH-Sensitive TRPA1 Activation in Odontoblasts Regulates Mineralization. J Dent Res. 95(9):1057-64.

Koori K, Maeda H, Fujii S, Tomokiyo A, Kawachi G, Hasegawa D, Hamano S, Sugii H, Wada N, Akamine A (2014). The roles of calcium-sensing receptor and calcium channel in osteogenic differentiation of undifferentiated periodontal ligament cells. Cell Tissue Res. 357(3):707-18.

Kyung T, Lee S, Kim JE, Cho T, Park H, Jeong YM, Kim D, Shin A, Kim S, Beak J, Kim J, Woo D, Chae S, Kim CH, Shin HS, Han YM, Kim D, Heo WD (2015). Optogenetic control of endogenous Ca^{2+} channels in vivo. Nat Biotechnol. 33(10):1092-6.

Lee JH, Lee DS, Choung HW, Shon WJ, Seo BM, Lee EH Cho JY, Park JC (2011). Odontogenic differentiation of human dental pulp stem cells induced by preameloblast-derived factors. Biomaterials. 32(36):9696-706.

Lee SJ, Monsef M, Torabinejad M (1993). Sealing ability of a mineral trioxide aggregate for repair of lateral root perforations. J Endod. 19(11):541-4.

Li S, Hu J, Zhang G, Qi W, Zhang P, Li P, Zeng Y, Zhao W, Tan Y (2015). Extracellular Ca^{2+} Promotes Odontoblastic Differentiation of Dental Pulp Stem Cells via BMP2-Mediated Smad1/5/8 and Erk1/2 Pathways. J Cell Physiol. 230(9):2164-73.

Li T, Sun M, Yin X, Wu C, Wu Q, Feng S, Li H, Luan Y, Wen J, Yan L, Zhao B, Xu C, Sun Y (2013). Expression of the calcium sensing receptor in human peripheral blood T lymphocyte and its contribution to cytokine secretion through MAPKs or NF-kB pathways. Mol Immunol. 53(4):414-20.

Law AS (2013). Considerations for regeneration precedures. J Endod. 39(3 Suppl):S44-56.

Maeda H, Nakano T, Tomokiyo A, Fujii S, Wada N, Monnouchi S, Hori K, Akamine (2010). Mineral trioxide aggregate induces bone morphogenetic protein-2 expression and calcification in human periodontal ligament cells. J Endod. 36(4):647-52.

Magno AL, Ward BK, Ratajczak T (2011). The calcium-sensing receptor: a molecular perspective. Endocr Rev. 32(1):3-30.

Namkoong E, Shin YH, Bae JS, Choi S, Kim M, Kim N, Hwang SM, Park K (2015). Role of Sodium Bicarbonate Cotransporters in Intracellular pH Regulation and Their Regulatory Mechanisms in Human Submandibular Glands. PLoS One. 10(9)

Parirokh M, Torabinejad M (2010a). Mineral trioxide aggregate: a comprehensive literature review--Part III: Clinical applications, drawbacks, and mechanism of action. J Endod. 36(3):400-13.

Parirokh M, Torabinejad M (2010b). Mineral trioxide aggregate: a comprehensive literature review--Part I: chemical, physical, and antibacterial properties. J Endod. 36(1):16-27.

Pi M, Faber P, Ekema G, Jackson PD, Ting A, Wang N, Fontilla-Poole M, Mays RW, Brunden KR, Harrington JJ, Quarles LD (2005). Identification of a novel extracellular cation-sensing G-protein-coupled receptor. J Biol Chem. 280(48):40201-9.

Quinn SJ, Kifor O, Trivedi S, Diaz R, Vassilev P, Brown E (1998). Sodium and ionic strength sensing by the calcium receptor. J Biol Chem. 273(31):19579-86.

Quinn SJ, Bai M, Brown EM (2004). pH Sensing by the calcium-sensing receptor. J Biol Chem. 279(36):37241-9.

Sangwan P, Sangwan A, Duhan J, Rohilla A (2013). Tertiary dentinogenesis with calcium hydroxide: a review of proposed mechanisms. Int Endod J. 46(1):3-19.

Sarkar NK, Caicedo R, Ritwik P, Moiseyeva R, Kawashima I (2005). Physicochemical basis of the biologic properties of mineral trioxide aggregate. J Endod. 31(2):97-100.

Sohn S, Park Y, Srikanth S, Arai A, Song M, Yu B,Shin KH, Kang MK, Gwack Y, Park NH, Kim RH (2015). The Role of ORAI1 in the Odontogenic Differentiation of Human Dental Pulp Stem Cells. J Dent Res. 94(11):1560-7.

Spurney RF, Pi M, Flannery P, Quarles LD (1999). Aluminum is a weak agonist for the calcium-sensing receptor. Kidney Int. 55(5):1750-8.

Sun W, Sun W, Liu J, Zhou X, Xiao Y, Karaplis A, Pollak MR, Brown E, Golzman D, Miao D (2010). Alterations in phosphorus, calcium and PTHrP contribute to defects in dental and dental alveolar bone formation in calcium-sensing receptor-deficient mice. Development. 137(6):985-92.

Tada H, Nemoto E, Kanaya S, Hamaji N, Sato H, Shimauchi H (2010). Elevated extracellular calcium increases expression of bone morphogenetic protein-2 gene via a calcium channel and ERK pathway in human dental pulp cells. Biochem Biophys Res Commun. 394(4):1093-7.

Torabinejad M, White DJ, inventors; Loma Linda University, assignee. Tooth lling material and method of use. United States Patent 5,415,547. 1995.

Torabinejad M, White DJ, inventors; Loma Linda University, assignee. Tooth lling material and method of use. United States Patent 5,769,638. 1998.

Torabinejad M, Parirokh M (2010). Mineral trioxide aggregate: a comprehensive literature review--part II: leakage and biocompatibility investigations. J Endod. 36(2):190-202.

Tsai FC, Seki A, Yang HW, Hayer A, Carrasco S, Malmersjo S Meyer T (2014). A polarized Ca^{2+}, diacylglycerol and STIM1 signalling system regulates directed cell migration. Nat Cell Biol. 16(2):133-144.

Wigler R, Kaufman AY, Lin S, Steinbock N, Hazan-Molina H, Torneck CD (2013). Revascularization: a treatment for permanent teeth with necrotic pulp and incomplete root development. J Endod. 39(3):319-26.

Yan M, Wu J, Yu Y, Wang Y, Xie L, Zhang G Yu J, Zhang C (2014). Mineral trioxide aggregate promotes the odonto/osteogenic differentiation and dentinogenesis of stem cells from apical papilla via nuclear factor kappa B signaling pathway. J Endod. 40(5):640-7.

Yasuda Y, Ogawa M, Arakawa T, Kadowaki T, Saito T (2008). The effect of mineral trioxide aggregate on the mineralization ability of rat dental pulp cells: an in vitro study. J Endod. 34(9):1057-60.

Zhao Y, Araki S, Wu J, Teramoto T, Chang YF, Nakano M, Abdelfattah AS, Fujiwara M, Ishihara T, Nagai T, Campbell RE (2011). An expanded palette of genetically encoded Ca^{2+} indicators. Science. 333(6051):1888-91.

Conclusion

- Calcium-sensing receptor (CaSR) is a major signaling mediator of Mineral trioxide aggregate (MTA)-induced biological reactions in human dental pulp cells (hDPCs).
- MTA activates diverse CaSR downstream pathways; notable, CaSR activation essentially requires dual modulation of extracellular Ca^{2+} and alkaline pH via MTA.
- Especially, Ca^{2+} mobilization from intracellular stores by the phospholipase C (PLC) pathway plays an important role in MTA-induced osteogenic differentiation by regulating transcriptional activity.
- My research shed light on the signal transduction mechanism of MTA, thus providing a crucial molecular basis for the use of MTA in regenerative dental therapy.

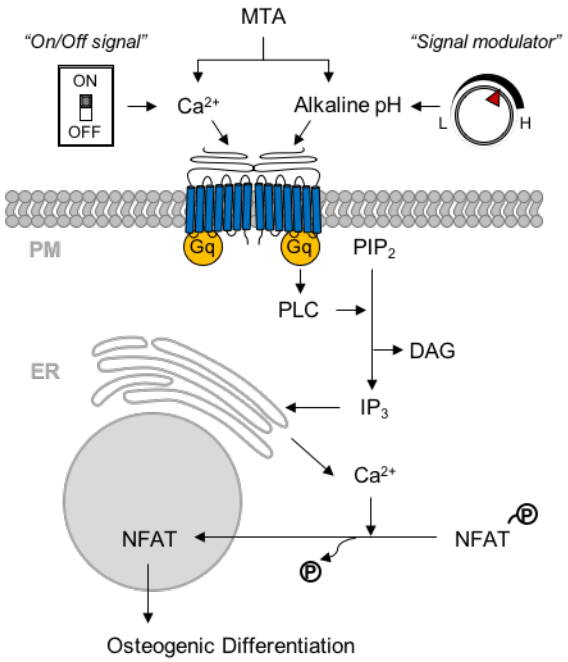

Figure 22. Schematic representation of MTA-mediated signaling pathways.

MTA activates CaSR downstream signaling upon the modulation of extracellular Ca^{2+} (which acts as an on/off signal) and pH (which acts as a signal modulator). The resultant intracellular Ca^{2+} mobilization via the PLC pathway induces NFAT activation, which leads to transcriptional changes in osteogenic differentiation.

국문초록

칼슘감지 수용체를 통한 mineral trioxide aggregate 의 세포 내 작용기전

최 슬 기

서울대학교 대학원 치의과학과 신경생물학 전공

(지도교수: 박 경 표)

Mineral trioxide aggregate (MTA)는 생활성 물질로 뛰어난 물성 및 다양한 임상적 효과로 인해 임상 치의학 분야에서 널리 사용되고 있다. MTA 는 감염에 노출된 치수의 회복과 상아질 형성을 유도하는 치수복조술, 근관 치료 과정에서 발생할 수 있는 천공부위의 밀폐작용으로 치근 주변조직의 회복 및 미성숙 영구치의 감염 시 치수강 내 혈관화를 유도하여 치근형성을 유도할 때 사용된다. 상기의 다양한 임상적 효능은 MTA 의 우수한 물리화학적 특성에 기인한다.

MTA 는 우수한 생체적합성, 밀폐성, 향균능력 등을 가지고 있으며 혈액 등 수분오염에도 뛰어난 저항성을 보여 다양한 임상적 효능을 보인다. 또한 MTA 의 적용으로 세포 증식, 면역 단백의 생산 및 분비, 분화 등 다양한 세포 내 활성이 보고되었다. 이런 효과를 통해 MTA 는 경조직 형성능력 및 생체조직의 재생 및 회복에 핵심적인 역할을 담당한다. 그러나 MTA 의 임상적인 효과에 대한 작용기전에 대해서는 MTA 의 생물학적인 활성화일 것이라고 생각하고 있을 뿐 실제적으로 세포 내에서 어떤 신호전달 과정을 거치는지에 대해서는 연구된 바가 부족한 실정이다. 생체친화적 물질인 MTA 의 세포 내 작용기전을 밝히는 연구는 치아 보존 치료의 적용에 있어 필수적이며, 생체 조직의 재생 및 회복과 관련되어 치의학 분야에서 꼭 해결해야 할 중요 연구과제이다. 이러한 점에 주목하여 본 연구를 통해 임상적 재생 치료에 있어 중요한 역할을 한다고 할 수 있는 MTA 의 세포 내 신호전달 작용기전에 대해서 연구하였다.

먼저 MTA 자극으로 인한 치수세포 내 칼슘 신호 변화를 관찰하였다. 세포 외부로부터 칼슘 유입이나 세포 내 칼슘 유리 경로를 차단하여 칼슘 증가의 경로를 보여줌으로써 기존에 밝혀지지 않았던 MTA 의 세포 내 칼슘 신호 경로를 제시하였다. 다음으로 MTA 의 신호전달 매개체로 칼슘감지 수용체 (Calcium-sensing receptor,

CaSR) 를 예상하고 이를 규명하기 위해 치수세포에서 칼슘감지 수용체의 발현을 확인하고, MTA 가 칼슘감지 수용체의 다양한 downstream pathway (PLC, Akt, ERK, NFAT) 에 관여함을 처음으로 밝혔다. 또한 MTA 의 수화반응으로 인한 칼슘 증가와 높은 pH 가 칼슘감지 수용체의 활성을 각각 조절하는 효과를 확인했다. 마지막으로 치수세포에서 칼슘감지 수용체의 기능적 발현을 확인하기 위해 MTA 에 의한 치수분화/골분화 관련 단백질의 발현을 검증하고 그에 따른 기전을 확인하였다.

종합해보면, 본 논문을 통해서 기존에 보고 되지 않았던 MTA 의 세포 내 신호전달 기전을 규명하였고, 칼슘감지 수용체를 통한 MTA 의 골분화관련 작용기전을 규명하였으며 치수세포에서 그 동안 보고되지 않았던 칼슘감지 수용체의 기능을 밝힘으로써 칼슘감지 수용체에 의해 유도되는 칼슘 신호에 따른 치수세포의 기능을 연구하는데 방향성을 제시하였다.

주요어: Mineral trioxide aggregate, 칼슘감지수용체, 칼슘, pH, 골분화, 치수세포

학번: 2010-23777